



Buckley Ellen (Orcid ID: 0000-0001-7415-5054)

Farrell Sinead, Louise (Orcid ID: 0000-0003-3222-2751)

Duncan Kyle (Orcid ID: 0000-0001-6959-1206)

## **Classification of Sea Ice Summer Melt Features in High-resolution IceBridge Imagery**

**Ellen M. Buckley<sup>1</sup>, Sinéad L. Farrell<sup>2</sup>, Kyle Duncan<sup>3</sup>, Laurence N. Connor<sup>4</sup>, John M. Kuhn<sup>4</sup>, and Roseanne T. Dominguez<sup>5</sup>**

<sup>1</sup>Department of Atmospheric and Oceanic Science, University of Maryland, College Park, MD.

<sup>2</sup>Department of Geographical Sciences, University of Maryland, College Park, MD. <sup>3</sup>Earth System Science Interdisciplinary Center, University of Maryland, College Park, MD. <sup>4</sup>NOAA Laboratory for Satellite Altimetry, College Park, MD. <sup>5</sup>Universities Space Research Association; NASA Ames Research Center, Moffett Field, CA.

Corresponding author: Ellen Buckley (buckley@umd.edu)

### **Key Points:**

- A novel algorithm is applied to IceBridge images of summer melt on Arctic sea ice, collected during surveys of two distinct ice regimes
- Distributions of sea ice concentration, melt pond fraction, and pond color for 2016 and 2017 reveal differences related to ice type
- Melt pond fraction was larger on first year ice, where dark ponds dominated, compared to multiyear ice, where light ponds were more common

This article has been accepted for publication and undergone full peer review but has not been through the copyediting, typesetting, pagination and proofreading process which may lead to differences between this version and the Version of Record. Please cite this article as doi: 10.1029/2019JC015738

## Abstract

High-resolution observations of melt ponds (MPs) across the Arctic are lacking, yet essential for understanding the sea ice energy budget and under-ice ecology. We present a pixel-based classification scheme to identify undeformed and deformed ice, open water, and light, medium and dark MPs in images of sea ice undergoing melt. The scheme was applied to 0.1 m-resolution Operation IceBridge Digital Mapping System imagery covering an area of  $\sim 4,000$  km<sup>2</sup>. Observations of both the unconsolidated, marginal ice zone of the Beaufort/Chukchi Seas (B/C Seas) and the consolidated, multiyear ice of the central Arctic (CA) were obtained. Sea ice concentration (SIC), melt pond fraction (MPF), and pond color fraction (PCF) were derived on a per-image basis. SIC averaged 69% in the B/C Seas, and 90% in the CA. We find that both MPF and PCF are dependent on the ice type on which ponds form. MPF averaged 25% in the B/C Seas, where dark ponds dominated and had a PCF of 60%, compared to a PCF of 9% and 31%, for medium and light ponds, respectively. MPF averaged 14% in the CA, where the PCF of light ponds was 68%, compared with 16% for both medium and dark ponds. As the multiyear ice of the Arctic Ocean is replaced by a younger, more seasonal ice cover, our results suggest that MPF will increase, and MP color will darken. This would enhance the ice albedo feedback, exacerbating that already due to the multi-decadal decline in summer ice extent.

## Plain Language Summary

Detailed observations of summer melt features on Arctic sea ice are limited, yet essential for modeling and understanding summer sea ice processes. An algorithm was developed to classify ice, open water, and melt ponds in high-resolution NASA Operation IceBridge Digital Mapping System (DMS) imagery. More than 17,000 images over  $\sim 4,000$  km<sup>2</sup> were analyzed. Sea ice concentration (SIC), melt pond fraction (MPF), and pond color fraction (PCF) were derived from the classified images. We compared results from two regions with distinct ice conditions: the unconsolidated marginal ice zone in the Beaufort and Chukchi (B/C) Seas, which consisted of predominantly first year ice, and the consolidated, predominantly multiyear ice pack of the central Arctic (CA) Ocean. In the B/C Seas, we found that the MPF is greater, SIC is lower, and ponds are darker than in the CA region. As the percentage of first year ice in the Arctic increases, our results suggest that the Arctic-wide MPF will increase, and pond color will darken. This will contribute to the positive ice-albedo feedback mechanism and has implications for modeling sea ice albedo.

## 1 Introduction

The 40-year satellite-derived record of Arctic sea ice extent reveals a negative and accelerating trend (-12.8% per decade) in the month of September at the sea ice minimum (Richter-Menge et al., 2019; Comiso, 2018). This decrease in summer ice extent has resulted in an increase in solar radiation absorption in the Arctic, spurring further ice melt through a positive feedback (Curry et al., 1995; see also Perovich et al., 2002a; Steele et al., 2010). Because of their lower albedo, melt ponds (MPs) that form on sea ice in summer absorb more incident radiation than un-ponded ice, enhancing the positive ice-albedo feedback. As the ice cover diminishes, MPs alter ocean-atmosphere heat fluxes, provide an additional source of moisture to the atmosphere (Boisvert et al., 2013), and impact under-ice ecology by increasing the transmission of light (Arrigo et al., 2012; Light et al., 2015; Horvat et al., 2017).

MPs were typically represented in global climate models through adjustment of the overall sea ice albedo in the summer months (Hunke et al., 2010). However, this does not account for variability in MPs with respect to regional ice type and sea ice topography, nor the observed range in MP albedo (Flocco et al., 2012), and an improved treatment of summer melt processes is required (Lüthje et al., 2006; Skyllingstad et al., 2009). Recent advances in parametrizing MPs have improved their representation in sea ice models (e.g., Flocco et al., 2010, 2012; Schröder et al. 2014), and in coupled ice-ocean models (e.g., Zhang et al., 2018). It has been shown that sea ice model predictions are sensitive to MP inclusion (Flocco et al., 2010; Flocco et al., 2012; Tsamados 2015), and simulations with MPs predict 13% lower minimum ice extent, and 40% lower ice volume, compared to those without ponds (Flocco et al., 2012). Schröder et al. (2014) also showed that MP fraction can be used to predict summer minimum extent. Rösel et al. (2012) found that early melt pond formation may contribute to the decline of September sea ice minimum extent.

The quantity and distribution of snow on sea ice, and sea ice topography, control the formation and evolution of summer melt ponds (Fetterer & Untersteiner, 1998). MPs manifest differently on first year and multiyear ice, as illustrated in Figure 1. Their albedo and color depend on pond depth, ice thickness, and sub-ice algal growth (e.g., Perovich et al., 1998; Light et al., 2015; Lu et al., 2018). Pond

albedo evolves throughout the melt season as ponds deepen and drain, ice porosity increases, ponds link to the ocean, and eventually refreeze (Perovich & Polashenski, 2012). Dark MPs typically found on first year ice have an albedo less than 0.2 (Perovich, 2017). Snow melt forms ponds which spread laterally across the level first year ice surface (Figure 1a) and can melt out the thin ice by the end of the season (Fetterer & Untersteiner, 1998). On multiyear ice pond albedo is  $\sim 0.35$  (Perovich, 2017). Since multiyear ice has an undulating topography due to a longer deformation and melt history, lateral spread of MPs across the surface is inhibited (Eicken et al., 2004; Petrich et al., 2012). Instead, drainage channels form, connecting ponds, allowing melt water to travel across the ice and pool in the lowest-lying topographic features (Figure 1b).

Here we consider the disparity between MP characteristics on first year and multiyear ice, given the context of a declining ice cover. The sea ice cover of the Arctic Ocean comprised  $\sim 55\%$  first year ice in 1985, which has increased to  $\sim 77\%$  in 2018 (Richter-Menge et al., 2019). As the ice transitions to a younger and thinner ice cover, we expect to see changes in MP areal fraction, albedo, depth, and volume. Incorporation of MP observations and processes in model simulations has produced differing outcomes for the trend in melt pond fraction (MPF): Schröder et al. (2014) showed an increase in MPF, while Zhang et al. (2018) showed no statistically significant trend in MPF per unit ice area. These diverging results indicate a need to reduce uncertainties in MP parameterization so as to better understand the impact of MPs on the sea ice energy budget. Thus, it is essential to continue to improve MP observations and summer melt process studies across the Arctic.

The majority of our understanding of MPs is derived from in situ field studies, particularly the Surface Heat Budget of the Arctic Ocean (SHEBA) program, a drifting ice camp in the Beaufort Sea from October 1997 to October 1998 (Uttal et al., 2002). SHEBA advanced the understanding of MP albedo, fraction and size distribution (Perovich et al., 2002a, Perovich et al., 2002b), and provided input for MPF and MP depth parameterization in modeling efforts (e.g. Curry et al., 2001). Airborne studies have demonstrated the ability to extract sea ice MP parameters from imagery but most are limited in spatial extent and temporal evolution. For example, Miao et al. (2015) classified images collected in the Arctic Pacific sector in one summer (2010) only, while Perovich et al. (2002b) and Tschudi et al. (2001)

analyzed aerial imagery collected during the 1998 SHEBA campaign. Wright and Polashenski (2018) demonstrated a classification algorithm using 66 images collected in the Beaufort and Chukchi Seas region in 2009, 2014, and 2016. Satellite imagery provides greater Arctic coverage, but often sacrifices resolution. Since MPs are of order 10 m<sup>2</sup> in area at melt onset (Perovich et al., 2002b) and expand in area throughout the melt season, high resolution imagery is required to resolve their geophysical features and evolution. Low resolution satellite imagery, while unable to resolve individual MPs, can provide information on MPF. Observations acquired by the Moderate Resolution Imaging Spectrometer (Rösel et al., 2012; Rösel & Kaleschke 2011; Tschudi et al., 2008), Medium Resolution Imaging Spectrometer (Istomina et al., 2015; Zege et al., 2015), Landsat-7 Enhanced Thematic Mapper (Markus et al., 2002, 2003), and Envisat advanced synthetic aperture radar imagery (Mäkynen et al., 2014), have proven useful for classifying summer sea ice features, determining melt pond fraction, and deriving sea ice albedo. The National Technical Means (NTM) 1 m resolution satellite imagery have been used for MP classification (Fetterer & Untersteiner 1998; Webster et al., 2015), but the satellites targeted specific strategic sites and the NTM database does not offer full coverage of the Arctic. Other commercial satellites such as the DigitalGlobe and Pléiades constellations also offer high resolution optical imagery but are limited in polar coverage (to 82°N) and data are only available under license. In summary, due to the current limitations in both widespread and detailed observations of MPs gaps remain in our knowledge of MP areal coverage, size, and distribution at an Arctic-wide level.

The current deficiencies in both observing and modeling MP characteristics at high resolution motivates our work to investigate the extraction of summer melt signatures from newly available airborne remote sensing data. The NASA Operation IceBridge (OIB) airborne mission obtained high-resolution measurements of the melt season in different regions of the Arctic in July 2016 and 2017. OIB was designed to fill the data gap between the ICESat (decommissioned in 2009) and ICESat-2 (launched in 2018) polar satellite missions, by collecting detailed surface measurements in the Arctic and Antarctic from multi-instrumented aircraft (Koenig et al., 2010). The spatial coverage, and detail, of the OIB observations allows for the investigation of sea ice properties at high resolution and over

larger length-scales than was previously possible. We investigate the utility of OIB summer observations to improve our understanding of sea ice melt processes and MP properties.

The paper is organized as follows: OIB campaigns and relevant datasets are described in Section 2. Quality control methodology, sea ice feature classification, and calculations of sea ice concentration (SIC), MPF, and pond color fraction (PCF) are detailed in Section 3. The results are presented in Section 4, followed by a discussion of regional variability and impacts of pixel misclassification on the derived products in Section 5. Concluding remarks are offered in Section 6.

## **2. Data**

### **2.1 NASA Operation IceBridge Summer Melt Surveys**

Two OIB sea ice campaigns occurred during the middle of the Arctic summer melt seasons of 2016 and 2017 (Figure 2). During these campaigns, the NASA 524 HU-25C Guardian aircraft operated at a nominal flight altitude of ~460 m and was equipped with a snow radar (Yan et al., 2017), laser altimeter (Krabill et al., 2002), and a digital camera (Dominguez, 2010), with positioning capabilities. The campaigns were conducted in different regions of the Arctic, exploring distinct ice regimes (Table 1). The July 2017 campaign was flown over the thickest and oldest multiyear ice in the Arctic, to the north of Canada and Greenland (Sallila et al., 2019), in the central Arctic (CA), where the Transpolar Drift pushes ice against the coast causing dynamic thickening (Haas, 2017) and a consolidated ice cover. The July 2016 campaign targeted mixed seasonal and perennial ice types in the Beaufort and Chukchi Seas (B/C Seas), where ice drift is influenced by the Beaufort Gyre, and much of the ice does not survive the summer melt season, resulting in a thinner and younger ice cover (Richter-Menge and Farrell, 2013).

#### **2.1.1 Airborne Imagery**

Here we use IceBridge Digital Mapping System (DMS) L1B Geolocated and Orthorectified Images (Dominguez, 2010) collected during the OIB Arctic summer campaigns. The DMS captured images every 5 seconds. At the nominal flight altitude, each image covers a surface area of ~ 575 m by

~ 400 m. DMS acquired 21 megapixel JPEGs with a Canon EOS 5D camera and Zeiss 28 mm lens. Each image was precisely tied to an Applanix 510 POS AV which captured time of exposure, location and attitude data. Image pixels were geolocated using ray trace algorithms incorporating aircraft movement (pitch, roll, heading) as well as lens distortion. The geolocated result was converted to the National Snow and Ice Data Center's polar stereographic map projection for the northern hemisphere. A JPEG 95% compression was applied, and the final image saved as a GeoTIFF. The geolocation process introduces expanded geographic coverage, portrayed as a black border of varying size around each frame. Each pixel within the image has a red, green, and blue channel value (RGB data), with a resolution of 0.1 m at nominal altitude (Dominguez, 2010).

Previously, DMS data were used for lead detection (Farrell et al., 2011; Onana et al., 2013), pressure ridge sail height measurements (Duncan et al., 2018), characterization of sea ice surface morphology (Newman et al., 2014), and roughness (Webster et al., 2015). We take advantage of the high resolution DMS data to classify sea ice surface types during melt, including small-scale features such as MPs and deformed ice. Continuous sampling throughout the flights allows for calculation of along-track parameters, including SIC and MPF.

## 2.2 Satellite Sea Ice Concentration

We examine sea ice concentration extracted from the DMS data (DMS SIC) in the context of two sea ice concentration datasets derived from satellite passive microwave radiometers. We use the AMSR2 Daily 12.5 km Sea Ice Concentration (AMSR2 SIC) product, created using JAXA Advanced Microwave Scanning Radiometer 2 (AMSR2) brightness temperatures processed with the NASA Team 2 algorithm (Meier et. al., 2018). We also compare with the lower resolution NOAA/NSIDC Climate Data Record of Sea Ice Concentration (CDR SIC), a 25 km product derived using the Special Sensor Microwave Imager/Sounder (SSM/I/S) brightness temperature measurements, and which, for each grid cell, selects the higher concentration value derived from the NASA Team and NASA Bootstrap algorithms (Meier et. al., 2017a).

### 3 Methodology

Our goal is to classify every DMS surface pixel into one of four ice-type categories: undeformed ice, deformed ice, open water and ponded sea ice (Figure 3). The DMS images are not routinely adjusted for scene brightness due to varying overhead cloud conditions and sun angle during flight, and are thus not uniformly lit. Therefore, it is essential that surface type classification criteria are not based on fixed thresholds. Rather, criteria are applied on a per-image basis, and automatically adjust to suit the specific brightness levels of each image. We utilize the RGB channel data provided in each DMS image ( $C_r$ ,  $C_g$ ,  $C_b$ ), and the normalized pixel value,  $C_n$ , defined as:

$$C_n = (C_r - C_g)/(C_r + C_g) \quad (1)$$

We analyze distributions (histograms) of pixel values in these channels using a bin width of 2 pixel values for the  $C_r$ ,  $C_g$ , and  $C_b$ , and 0.02 for  $C_n$ , to ensure high resolution such that the frequency distribution can be determined. Modes are defined as a collection of bins bounded by pixel count minima on either side. The modal value is defined as a bin with lower pixel counts on either side. The difference between pixel count on either side of a modal value must be greater than 0.05% of the total number of pixels counted in the histogram. This is to eliminate the detection of erroneous modes. The maxima (ma) are annotated as follows:  $C_xma_y$  where x is r (red), g (green), b (blue), or n (normalized) and y is the mode number, counting from 1, the modal value with the lowest pixel values, to m, the modal value with the highest pixel values. For example, the second mode in  $C_r$  is labeled  $C_rma_2$ . Similarly, the minima (mi) are defined as a bin with higher pixel counts on either side and are labeled  $C_xmi_y$ . We also calculate the half maximum (hm) and quarter maximum (qm) of the mode on the left (L) or right (R) side of the mode. The half (quarter) maximum is the bin at which the pixel count is equal to 0.5 (0.25) of the pixel count in the associated mode. For example, to denote the half maximum bin value on the left side of the second mode in the blue channel, we write  $C_bma_2hm_L$ .

### 3.1 Quality Control

Prior to preprocessing and classification, we perform a data quality assessment to ensure consistency in our analysis for obtaining robust results. Metadata associated with each image provide image acquisition time, latitude, longitude, pixel size ( $ps$ ), and aircraft pitch ( $A_p$ ) and roll ( $A_r$ ). At a nominal flight altitude of 460 m,  $A_p = 0^\circ$  and  $A_r = 0^\circ$ ,  $ps = 0.1$  m. We retain only those images acquired under nominal flight conditions, eliminating any images collected during aircraft maneuvers, by selecting data with the following attributes:  $ps < 0.25$ m, and  $A_r, A_p < \pm 5^\circ$ . These filtering steps ensure that each pixel represents a consistent surface area, simplifying calculations of the area of each sea ice parameter derived from the classified pixels. In addition, since the algorithm is designed for classification of ocean and sea ice features only, images containing clouds and land are identified by visual inspection and manually removed from the data set.

The quality control results show long sections of flight obscured by clouds, eliminating many consecutive images from analysis (Figure 4). Non-nominal values of parameters related to aircraft maneuvers, like pitch and roll that are required to align the aircraft along pre-defined survey lines, are observed in discrete sections of the flights. During one leg of the 24 July 2017 flight (images 400-2400), the pitch oscillated around  $5^\circ$  (Figure 4). We eliminate all images in this region (a total of 783 images), to ensure the non-nominal pitch in this section does not impact the results. The images discarded when pixel size is larger than the nominal value are found at the beginning and end of flights, as the aircraft ascends to a higher altitude for transit to and from the base. Of the total 46,162 DMS images collected during 11 flight surveys (Table 1), 8.9% were eliminated due to roll, 6.6% due to pitch (including those eliminated in the 24 July 2017 flight segment), and 9.2% due to altitude outside of nominal conditions. Upon manual inspection, 37.5% were discarded due to the presence of clouds obscuring surface features, and less than 1% of images were eliminated due to contamination by land. In total, 17,217 images (37.3% of total data collected) remained for the next step, image preprocessing.

The data quality control may introduce some statistical biases to the processed dataset. Clouds and sea smoke may preferentially form over areas of open water with a lower ice concentration, due to

abundance of available moisture. Therefore, discarding data in cloudy regions may not fully capture the amount of open water on the survey line, biasing the dataset towards a conclusion of higher sea ice concentration.

### 3.2 Image Preprocessing

A black border surrounds the surface pixels in each DMS image and is used to mitigate the effects of variations in aircraft pitch, roll, and altitude, on the resulting shape of the image projected to the Earth's surface. The number of black border pixels surrounding the surface pixels is variable between images. As a first, preprocessing step, we identify and eliminate border pixels in each GeoTIFF so that we analyze only the surface pixels that are associated with the sea ice and ocean surface (Figure 5). We cannot simply remove border pixels using a set color threshold of zero (black), however, because border pixels near the edge of the surface pixels have brightness values greater than zero as a result of image projection (Section 2.1.1). These border pixels may also have brightness values that coincide with the brightness values of some surface pixels (e.g. open water). Therefore, we identify the corner points of the array containing the surface pixels as the first pixel from left to right and top to bottom with  $C_r > 4$  (Figure 5a). Pixels outside of the lines connecting these corner points are identified as border and discarded from further analysis. Due to the georeferencing of the images some border pixels may remain within these lines after the first iteration and require further identification (Figure 5b). We examine a histogram of the remaining pixels (Figure 5c) and eliminate pixels  $C_b < C_{bmi_1}$ . All remaining pixels are classified as surface pixels (Figure 5d) and are further categorized by ice-type in the following steps.

The 17,217 images remaining after quality control were preprocessed to identify surface pixels. For 2 images (0.01% of total data), image preprocessing was unsuccessful, and corner points delineating surface and border pixels were not located. These images did not proceed to the classification steps. On average, there are 22.9 million surface pixels per image, with a standard deviation of 2.3 million pixels. Based on the expected number of classified pixels, we identified any results that suggested the algorithm

did not perform as intended during the preprocessing, flagging images with surface pixel counts that deviated by more than 1-sigma about the average, i.e. outside the range of 20.6 – 25.2 million pixels. This resulted in a total of 182 flagged images which were not used in the analysis. Upon inspection, we found that the failure occurred during the second preprocessing step (Figure 5c). Of the 182 flagged images, 166 images (91%) contained open water pixels along the edge between the surface and border pixels which were misidentified as border pixels, resulting in too few surface pixels. In this step the pixels less than  $C_{bmi_1}$  are classified as border pixels. If the open water pixels and border pixels occupy one mode ( $C_{bma_1}$ ), when the mode is classified as border pixels, the open water pixels in that mode are misclassified as border pixels. The rest of the flagged images (16 images, 9%) had more than 25.2 million surface pixels. In these cases, the algorithm did not correctly find the corners of the image, and many border pixels were misidentified as surface pixels. Following image preprocessing, 17,033 images remained for feature classification.

### 3.3 Feature Classification

After the quality control filtering and preprocessing steps (as outlined in Sections 3.1 and 3.2), surface pixels within the remaining 17,033 DMS images are classified (Figure 6a). We hypothesize that each of the four sea ice classes (undeformed ice, deformed ice, open water and ponded sea ice) has a unique signature in  $C_r$ ,  $C_g$ ,  $C_b$ , and  $C_n$ , and it is therefore feasible to classify individual pixels based on the values of the RGB channel data relative to other pixels in the image. The algorithm was developed using a test image set (available in the supporting information, Figures S1-S40). Forty images were selected from the database encompassing a full range of ice types encountered during the summer melt surveys, including fully consolidated multiyear ice, predominantly open water, heavily ponded ice floes, thaw holes, un-ponded ice floes, level first year ice, heavily deformed multiyear ice, images with overhead clouds, a range of melt pond sizes and colors, melting snow, very thin ice, and deformed ice with evidence of cracks, algae, and/or slush (Table S1).

### 3.3.1 Sea Ice

Snow-covered sea ice has high RGB values that are similar in all three channels resulting in bright, neutral-colored white surfaces. When ice floes collide, the ice surface deforms, breaking into blocks and creating pressure ridges and rubbled ice. Some faces of the broken ice blocks are oriented towards the sun at the time of flight, resulting in the brightest surface relative to all other surface pixels.

In the  $C_r$  histogram, ice pixels occupy the highest bins and form a distinct mode,  $C_r ma_m$ . In images with significant amounts of deformed sea ice, there are two high-value modes in the red channel histogram ( $C_r ma_m$  and  $C_r ma_{m-1}$ ) (Figure 6b). If deformed ice is present, the highest value modes in the red channel are within 10 bins of each other, i.e.,  $(C_r ma_m - C_r ma_{m-1}) \leq 10$ , and both modes are associated with ice pixels (Figure 6b). In this case, threshold B is defined as the first bin to the right of  $C_r ma_m$  that is less than half of the pixel count in the modal value bin ( $C_r ma_m hm_R$ , Figure 6b).

$$B = C_r ma_m hm_R \quad (2)$$

Threshold C is set as the minimum to the left of the second highest mode (Figure 6b):

$$C = C_r mi_{m-1} \quad (3)$$

In the case where no deformed ice is present, i.e., where  $(C_r ma_m - C_r ma_{m-1}) > 10$ , threshold B is set as the maximum pixel value in the red channel:

$$B = \max(C_r) \quad (4)$$

and threshold C is defined as:

$$C = C_r mi_m \quad (5)$$

After setting thresholds B and C depending on the presence of deformed ice, we classify all snow-covered ice pixels with  $C_r \geq C$ , and further classify undeformed ice pixels as ice pixels with  $C_r < B$ , and deformed pixels as  $C_r \geq B$  (Figure 6c).

In these steps some MP pixels are misclassified as ice (Figure 6d). These misclassified pixels are located in the lightest MPs, i.e., shallow ponds with thick ice draft below. To separate MP pixels

from ice pixels, we introduce another requirement to refine the ice mask (second iteration). MPs have high green and blue channel values compared to their red channel values; hence MP pixels have lower normalized pixel values ( $C_n$ ) than ice pixels. In the second iteration, we analyze the  $C_n$  histogram of all surface pixels, and if there is only one mode, threshold  $D$  is set as the mode minus two times the difference between the mode and the half maximum on the left:

$$D = C_n m a_1 - (2 \times (C_n m a_1 - C_n m a_1 h m_L)) \quad (6)$$

If there is more than one mode (Figure 6e), we identify the mode that has the highest pixel count (i.e. the location of the maximum  $C_n$  bin) as  $C_n m a_y$ , where  $y = 1, 2, 3, \dots, m-1, m$ , in the  $C_n$  histogram. Threshold  $D$  is set as the minimum to the left of  $C_n m a_y$  (Figure 6e):

$$D = C_n m i_y \quad (7)$$

All pixels with  $C_n \leq D$  are removed from the ice mask (Figure 6f). For the example provided in Figure 6, a total of 286,305 pixels (1.2% of surface pixels) were removed in the second iteration (Figure 6g). The ice classification is complete and the remaining pixels move on to the next classification step.

### 3.3.2 Open Water

We define two water classes: melt pond (MP) and open water (OW). These two classes are often difficult to distinguish and define. Here, we define MPs as ponded freshwater on the sea ice surface. As soon as the ponded water melts through the ice and exposes the open ocean, it is considered open water since those melted-through ponds have the same pixel values as open water in all channels. Open water has the lowest value in all channels. Open water is found beyond the ice edge, in leads between ice floes, and in ponds that have completely melted through the ice.

To detect open water, we use the blue channel,  $C_b$  (Figure 7a). If present, open water pixels occupy the lowest value pixels in the blue channel ( $C_b m a_1$ ) and form a distinct narrow mode. If the quarter maximum to the left of the lowest value mode ( $C_b m a_1 q m_L$ ) is fewer than 6 bins from the lowest value mode, there is open water in the image. In some cases, the open water pixels can occupy two

closely-spaced, low-value pixel modes. For all the modes within 8 bins of  $C_b m a_1$ , we define threshold  $E$  as the first minimum at a higher pixel value than the highest pixel value mode of these modes (Figure 7a), i.e.,

$$C_b m a_z = \max(C_b m a_x \mid (C_b m a_x < (C_b m a_1 - 8))) \quad (8)$$

$$E = C_b m i_z \quad (9)$$

Where  $x, z$  are 1, 2, 3, ...,  $m-1, m$ , in the  $C_b$  histogram. A threshold width of 8 bins was determined empirically and ensures that the mode selected is a low  $C_b$  value. If there is no open water present in the surface pixels, threshold  $E = 0$ . If there are no minima (Figure S41a),  $E$  is defined relative to the mode:

$$E = C_b m a_x + 3(C_b m a_x h m_R - C_b m a_x) \quad (10)$$

Open water is classified as all the unclassified pixels with  $C_b < E$  (Figures 7b and S41b). Pixels with  $C_b \geq E$  are classified as MP pixels and are further classified in the next step.

### 3.3.3 Melt Ponds

After identification of deformed ice, undeformed ice and open water pixels, all remaining pixels are classified as MPs (Figure 7b). MPs range in color from light to dark blue, depending on the depth of the pond and the properties of the underlying ice (Eicken et al., 2004). Lighter ponds tend to have thick ice below and, as their depth increases, their color darkens. Due to the requirement of thick ice below, the lightest MPs are more common on thick, multiyear ice than on thinner, first-year ice.

Here, MP pixels are further distinguished as light (LMP), medium (MMP), and dark ponds (DMP). For the classification of MP type, we utilize the blue channel ( $C_b$ ) histogram (Figure 8a). Because MPs can range in color from dark to light blue,  $C_b$  has the widest spread of pixel values associated with MPs. Low  $C_b$  values indicate dark MPs, and high  $C_b$  values indicate light blue MPs. The MP color classification is based on the  $C_b$  values of the unclassified pixels relative to the values of ice and open water in the image. We calculate the average value of the ice ( $\overline{ice}$ ) and open water ( $\overline{ow}$ )

pixels in the image that were identified in the steps described in Sections 3.3.1 and 3.3.2. We establish the baseline thresholds for dark, F, and light, G, MP pixels as 40% and 60%, respectively, of the difference between  $\overline{ow}$  and  $\overline{ice}$  added to  $\overline{ow}$  (Figure 8a).

$$F = \overline{ow} + 0.4 * (\overline{ice} - \overline{ow}) \quad (11)$$

$$G = \overline{ow} + 0.6 * (\overline{ice} - \overline{ow}) \quad (12)$$

Next, we refine these thresholds based on the location of the modes in the  $C_b$  histogram (Figure 8a). We classify modes based on their location relative to these two values. Modes are classified as dark MP modes where  $C_{bmax} < F$ , medium MP modes where  $F \leq C_{bmax} < G$ , and light MP modes where  $C_{bmax} \geq G$ .

If any dark MP modes exist, a new threshold for dark MP pixels, F, is set as the minimum to the right of the highest pixel value dark MP mode. Likewise, the threshold for light MP pixels, G, is set as the minimum to the left of the lowest pixel value light MP mode:

$$C_{bma_p} = \max(C_{bma_x} | C_{bma_x} < F) \quad (13)$$

$$C_{bma_q} = \min(C_{bma_x} | C_{bma_x} \geq G) \quad (14)$$

$$F = C_{bmi_p} \quad (15)$$

$$G = C_{bmi_q} - 1 \quad (16)$$

After determining these thresholds, we classify dark MPs as  $C_b < F$ , medium MPs as  $F \leq C_b < G$ , and light MPs as  $C_b \geq G$  (Figure 8b). This step concludes the classification algorithm process; all surface pixels have now been classified.

### 3.3.4 Classified Images

Classified images are stored as HDF dataset matrices with the dimensions of the GeoTIFF and the integer value corresponding to the ice-type classification category: border (0), undeformed ice (1),

deformed ice (2), open water (3), DMP (4), MMP (5), and LMP (6). There are no unclassified pixels. Figure 9 shows an example of the raw DMS data (Figure 9a) and the final classified image (Figure 9b).

### 3.3.5 Pixel Misclassification

Although the classification algorithm includes steps to differentiate hard-to-distinguish features, instances of pixel misclassification persist (Figure 10). Geophysical features occurring during the melt season that are not classified by the algorithm include ridge shadows, sun glint, and ice draft. The algorithm is designed to minimize errors based on its performance on the test image set (Supplementary Information 1). Here, we briefly consider each of the common potential pixel misclassifications and discuss their impact.

1. Ridge shadows: The RGB values of ridge shadows fall in the middle of the spectrum, between the low values of open water and the high values of ice, and are similar to MP RGB values. Ridge shadows exhibit a higher, but overlapping,  $C_n$  value compared to MPs, and thus most are separated from pond pixels in the algorithm (Figure 6e), but some misclassifications persist (Figures 10a, S17, S22, S27). The results (Table 2) show that deformed ice comprises on average 0.5% of surface pixels, whereas MP pixels comprise 15.4% on average. Assuming the number of misclassified ridge shadow pixels are less than or equal to the number of deformed ice pixels, ridge shadows can contribute a maximum MP pixel error of 0.5%.
2. Sun glint: At the high end of the intensity spectrum, sun glint pixels in water are classified as ice or melt pond. When sunlight reflects off an open water disturbance, it can result in a specular reflection into the camera lens which saturates the RGB values of those pixels. In our current algorithm, white pixels resulting from sun glint are misclassified as ice or dark melt ponds (Figures 10b, S3). However, sun glint appears only in large areas of open water which are uncommon in our study region. We determined that sun glint is present in less than 5% of all images analyzed. We looked at three images where sun glint in open water occurred and found 2% of open water pixels were

misclassified as ice or MPs. Therefore, we conclude that sun glint is a minor issue, and can contribute a maximum MP pixel error of  $\ll 1\%$ .

3. Ice draft: It is difficult to distinguish ice draft from MPs in the pixel-based, RGB-sensitive, algorithm (Figure 10c, S11, S12, S18, S31). The algorithm does not attempt to remove ice draft pixels from the MP pixels. Ice draft is visible along ice edge floes, which are prevalent in images of unconsolidated ice due to a higher percentage of individual ice floes (resulting in a longer, aggregated floe perimeter), but can occur in any image. To quantify this error, we look at images with SIC  $< 80\%$  (33% of all processed images). On average, 10% of pixels within these images are classified as melt pond pixels. Therefore, we can conclude that this misclassification has a moderate impact on images with SIC  $< 80\%$  and has a minor impact on images with SIC  $\geq 80\%$ .
4. Open water in close proximity to dark melt ponds: Open water and dark melt ponds have similar RGB values, and in images with both, there may be a natural break (minimum) in the  $C_b$  histogram between the features (e.g. Figure 7, Threshold E, Equation 9). For 1,858 images (11% of processed image), no minima in the  $C_b$  histogram are found and Threshold E is determined relative to the mode (Equation 10, Figure S41). Misclassification of open water pixels as dark melt pond may occur during this step (Figures 10d, S16, S20, S28, S41). To quantify the potential impact of this misclassification, we consider the statistics associated with DMP pixels in these images. We find the percentage of DMP pixels per image ranges from 0 to 24% and is on average 4% with a standard deviation of 5%. These results suggest that potential misclassification of OW pixels as DMP pixels would only occur infrequently. Since this potential misclassification can impact a maximum of 11% of the data and is expected to occur infrequently, we conclude that it has minimal impact on the derived products.
5. Very light melt ponds: In the early stages of melt pond formation, as the snow melts and meltwater collects into pools, the ponds are very light in color and may be misclassified as ice (Figures 10e, S30, S38). The second iteration of the ice classification step (Equations 6 and 7) was introduced to rectify this misclassification by removing light melt pond pixels from the ice mask (Figure 6d). In the second iteration, on average, 3% of ice pixels were removed from the ice mask and classified

as melt pond pixels. With this additional iteration to refine the ice step, we expect this misclassification is infrequent and has minimal impact on the results.

Grouping pixels into object sets and considering geometric thresholding may improve the accuracy of classification and resolve some of the aforementioned misclassification errors. However, introducing these approaches in the current algorithm would increase computational processing time and may result in additional, unforeseen pixel misclassification errors. Because we did not consider any of these issues to impact the majority of the data, we did not implement any further steps to mitigate potential pixel misclassification.

In summary, we conclude that pixel misclassifications due to cases 1, 2, 4 and 5 are minor and do not significantly impact the results. Case 3 could potentially have a larger impact on the derived parameters (SIC and MPF) and this is further discussed in Section 5.2.

### 3.4 Derived Summer Melt Parameters

After the classification of each surface pixel, we derive summer melt features on sea ice by taking ratios of ice-type pixels. SIC, MPF and PCF are derived on a per-image basis, thus taking advantage of the highest resolution available.

#### 3.4.1 Sea Ice Concentration

WMO (1970) defines SIC as “the amount of the sea surface covered by ice as a fraction of the whole area being considered.” Here, we calculate the percentage and define SIC as:

$$SIC = \frac{MP + ICE}{MP + ICE + OW} \times 100 \quad (17)$$

### 3.4.2 Melt Pond Fraction

MPF is the ponded area relative to the sea ice area (Webster et al., 2015). We define MPF as the ponded percentage of the sea ice area:

$$MPF = \frac{MP}{MP + ICE} \times 100 \quad (18)$$

Here we calculate MPF for all data collected within the ice pack, defined as areas where SIC > 15%. This minimizes the effects of submerged ice draft or brash ice contributing to the MPF parameter close to the ice edge.

### 3.4.3 Pond Color Fraction

We calculate PCF as an additional statistic to normalize the pond color pixels by the total melt pond pixels per image. The number of surface pixels in each pond color classification type (light, medium, dark) is divided by the total number of MP pixels in the image to determine the make-up of pond color within the image:

$$PCF_D = \frac{DMP}{DMP + MMP + LMP} \times 100 \quad (19)$$

$$PCF_M = \frac{MMP}{DMP + MMP + LMP} \times 100 \quad (20)$$

$$PCF_L = \frac{LMP}{DMP + MMP + LMP} \times 100 \quad (21)$$

## 4 Results

### 4.1 Feature Classification

The percentages of surface pixels classified in each ice-type category were automatically calculated on a per-image basis for 17,033 images, covering an area  $\sim 4,000$  km<sup>2</sup> in size. Table 2 summarizes the classification statistics averaged per flight, both in terms of the percentage of ice type categories, and the derived data products (SIC and MPF). Open water percentages in the B/C Seas surveys over the marginal ice zone (MIZ) (19%-38%, Table 2), are much greater than those in the CA region in the consolidated ice pack (4-16%, Table 2). MP color classification percentages are also related to the regional ice types; dark MPs are more prevalent in the B/C Seas region on first year ice, light MPs are more prevalent in CA region of multiyear ice (Table 2). The highest percentage of dark MPs (17%, Table 2) was found on 15 July 2016, a flight conducted entirely south of 75°N, in an area well into the melt season (Anderson et al., 2019). MPF results are further discussed in Section 4.3.

We examine the along-track variability in the percentage of sea ice (deformed and undeformed), open water, and MPs (light, medium, dark), per image in the flight profiles. The along-track classification is more variable in the B/C Seas than in the CA (Figures 11a and b). Large deviations in the percentage of open water in the B/C Seas are observed (blue line, Figure 11a), and increases to 100% for a stretch of images during the 19 July, 2016 flight. More along-track consistency in the surface classification percentages is observed in the CA. There, ice cover characteristics are less variable, with consistently low percentages of OW pixels (between 0% and 20%) and high percentages of ice pixels throughout the flights (between 60% and 100%). The exception is the 24 July, 2017 flight which sampled the Lincoln Sea polynya at the northern limit of the Nares Strait, where a large area of open water contributed to a high flight-averaged open water percentage of 16% (Table 2). The percentage of melt pond pixels per image is dependent on the amount of ice in the image. The MP pixel percentage in the B/C Seas ranges from 0 - 50%, exhibiting high variability in MP pixels per image, because of the high variability in SIC in this region. The flight averaged MPFs in this region range from 16 % to 32%

(Table 2). The highest MP percentages, and highest MPF (32%, Table 2) were observed during the 15 July 2016 survey (Figure 11a). MP areal percentages are lower and less variable in the CA at ~20%, resulting in flight-averaged MPFs that range from 10% to 16% (Table 2).

Next we consider the MP color classification, which reveals regional differences in pond type. The along-track profiles allow us to examine the variability as the flight traverses the ice cover (Figures 11c and d), while the histograms provide a summary of the PCF for the entire season (Figures 11e and f). Dark MPs are the predominant MP type in the 2016 surveys over the B/C Seas (Figure 11e), with the exception of the flight on 13 July, 2016 (Figure 11c). The two flights that exhibit the highest fraction of dark MPs ( $PCF_D = 79\%$  and  $65\%$ ), (Figure 11c), are located in the Chukchi Sea. In contrast, light MPs prevail in the CA region (Figure 11f). Only a small segment of the 25 July 2017 (a) flight had more dark MPs than light MPs (Figure 11d). On average in the B/C region,  $PCF_D$  was 60%,  $PCF_M$  was 9%, and  $PCF_L$  was 31% (Table 2, Figure 11e). In the CA region  $PCF_D$  was 16% on average,  $PCF_M$  was 16%, and  $PCF_L$  was 68% (Table 2, Figure 11d). These results confirm that MP color is closely related to the ice type on which the MP forms.

#### 4.2 Sea Ice Concentration

Following pixel classification, and applying Equation 17, we determine the SIC per image (Table 2, Figure 12). The high resolution of the parameters results in a wide range of values, because some images contain no open water, while others are 100% open water. We examine the 5<sup>th</sup> and 95<sup>th</sup> percentile of the SIC and MPF parameters rather than the minimum and maximum values, as they provide a more robust indication of the range. It is interesting to note that the 95<sup>th</sup> percentile SIC of all flights was 100% (Table 2), as the flights were designed to find and measure sea ice. However, the 5<sup>th</sup> percentile provides more detail about the regional setting, with low values in 2016 in the B/C Seas, which sampled the MIZ, an area of the ice cover affected by waves between the ice edge and the consolidated ice pack (WMO, 1970), and higher values for 2017 in the CA region, which sampled the consolidated ice pack. The average SIC of all the images during the summer surveys was 79%, with a

standard deviation of 28% (Table 2). Average SIC was 69% in the B/C Seas and 90% in the CA, with standard deviations of 32% and 15%, respectively (Table 2). The B/C Seas flight-averaged SIC ranged from 62% to 81%, and the lowest flight-averaged SIC was observed during the July 13, 2016 survey. Mapping the SIC for that flight line, which occurred along longitude  $-150^{\circ}\text{W}$ , shows that the survey crossed large areas of open water at the ice edge (Figure 2 and 11a), which reduced the flight-averaged SIC. The 5<sup>th</sup> and 95<sup>th</sup> percentiles of SIC for this flight are 0% and 100%, respectively, confirming that this flight sampled both open water areas and the consolidated ice cover. Conversely, the 2017 campaign was conducted almost entirely within the consolidated ice pack, and flight-averaged SIC ranged from 84% to 96%, with the highest concentrations observed during the survey on July 18, 2017 (Table 2). However, we note that many of the images from this flight were eliminated due to clouds (46.8%) or aircraft roll (25.8%), leaving only 158 images for analysis (Figure 4). The lowest flight-averaged SIC of 2017 occurred on 24 July, a flight sampling the Lincoln Sea and northern Nares Strait. The flight samples a long stretch of open water (the Lincoln Sea polynya) at the northern limit of the strait, reducing the average SIC observed during this flight survey (Figure 12b). The variability of SIC in this flight is demonstrated in Figure 12c, where an image at  $83.4^{\circ}\text{N}$ ,  $-59.9^{\circ}\text{W}$  with 65% SIC, is compared with an image at  $83.9^{\circ}\text{N}$ ,  $-59.6^{\circ}\text{W}$ , with 100% SIC (Figure 12d).

We examine the SIC distributions for the B/C Seas and CA regions in the context of satellite-derived measurements. A wide range of DMS SIC is evident as mapped on top of the AMSR2 SIC (Figures 12a and b), and demonstrated in Figures 12c and d. We extracted the daily AMSR2 SIC and CDR SIC values on the same date and at the same location as each DMS image acquired along the OIB flight lines (Figure 12e and f), demonstrating that all data products exhibit the same regional characteristics. Our results show consistency between the DMS-derived SIC and the satellite data sets in terms of mean and modal SIC and overlapping distributions of SIC (Figures 12e and f) for both regions surveyed. In both regions, the modal SIC was 95-100% for all three products. In the B/C Seas region a secondary mode exists with similar modal values for all three products (DMS SIC 75-85%, AMSR2 SIC 70-75%, CDR SIC 75-80%, Figure 12e). The average AMSR2 and CDR SIC in the B/C Seas are consistent at 82% and 81%, respectively, and on average, 12% greater than DMS SIC, which

is 69% (Figure 12e). AMSR2 SIC and CDR SIC in the B/C Seas have wider distributions (Figure 12e), than in the CA region (Figure 12f), where more than 90% of the satellite-derived data have a SIC of 95% or more.

The AMSR2 SIC in the CA region shows almost entirely 100% ice concentration with the exception of the site of the Lincoln Sea polynya at the north of the Nares Strait, whereas the higher-resolution DMS SIC shows there are other areas of lower ice concentration (Figure 12b and f). In the CA region, the mean value for DMS SIC was 9% less than the average satellite derived product. Due to the lower resolution, the satellite-derived products (AMSR2 SIC at 12.5 km, and CDR SIC at 25 km) cannot resolve the smallest areas of open water and thus do not capture the variability of the area that is evident in the DMS SIC results (Figures 12a, b, e and f). The lowest resolution product, CDR SIC has no ice free grid cells in the campaign region, with 35% - 40% as the lowest SIC. In the CA all three products agree in terms of a modal value of 100% SIC, however, the DMS SIC is a continuous distribution ranging from 60% to 100%. Previous validation of the AMSR2 SIC has shown a positive bias of 3.9% (Meier et al., 2017b), which is consistent with the CA results shown here.

#### 4.3 Melt Pond Fraction

Implementing Equation 18, we calculate MPF per image. On average, the MPF was 25% in the B/C Seas, and 14% in the CA region, with standard deviations of 15% and 6%, respectively (Table 2). The highest flight-averaged MPF was 32%, occurring 15 July, 2016. This flight surveyed sea ice in the Chukchi Sea, at the western limit of the aircraft range from Utqiagvik (Figure 13a). The entire flight line was south of 75°N, and surveyed areas of ice where the melt season was well underway. Here ponds have fully developed and have laterally spread across ice floes. Conversely, the lowest flight-averaged MPF is 10%, which occurred during the flight on 17 July, 2017, over the area north of Greenland and the Canadian Archipelago, an area of known ice convergence (Kwok, 2015), due to coastal boundaries that restrict ice motion (Figure 13b). Here, pressure ridges restrict the lateral spread of MPs (Figure 13c and d) and contribute to lower MPF. The 17 July, 2017 flight was repeated one week later on 25 July,

where the flight-averaged MPF was 14%, an increase of 4% over the survey of the same region one week earlier, demonstrating the temporal evolution of MPF in the CA region.

In our study MPF ranges from 16 - 32%, with an average of 25% (Table 2). This is consistent with the magnitude and variability of MPF found in previous studies. For example, Perovich et al. (2002b) found a mean MPF of 18.8% in the northern Chukchi Sea in July, 1998 with variability between 5% to 50% (Perovich et al., 2002b). Rösel and Kaleschke (2012) found MPFs of 40-50% in the B/C Seas in mid-July 2011. Webster et al. (2015) found MPFs ranging from 30% to 50% in a study area on first year ice in the southern B/C Seas.

We found an average MPF of 14% in the CA region in mid-July 2017 (Table 2, Figure 13b), slightly lower than previous studies have reported. For example, Rösel and Kaleschke (2012) reported MPFs ranging from 25-35% in mid-July 2011 in the CA region, north of Greenland and Ellesmere Island, Mäkynen et al. (2014) found MPFs ranging from 22% to 43%, averaging 34% in July, 2009 in the Greenland Sea to the northeast of Station Nord, and Istomina et al. (2015) found MPFs ranging from 10% to 30% north of Greenland in mid-July, 2009. We also demonstrate the reliability of our DMS results, by evaluating DMS-derived MPF with MPF derived from a Sentinel-2 image that is coincident with a section of a flight line in the Lincoln Sea over mixed sea ice conditions. On 24 July, 2017, Sentinel-2 captured imagery of the Lincoln Sea and northern Nares Strait, near coincident in time to a 57 km segment of the DMS survey that occurred the same day (delta time = 4.5 hours). To assess algorithm performance, we apply the classification algorithm to a 5 km wide strip of Sentinel-2 True Color Imagery (TCI) centered on the 57 km-long section of the DMS survey. We split the Sentinel-2 TCI into 57 Sections (1 km long x 5 km wide) and compared the classification results with 398 spatially-coincident DMS images in this region (Figure 13f). The results show strong agreement in the MPF distribution derived from both DMS and Sentinel-2 imagery, which is asymmetric in both cases with a modal MPF value of 10-15% (Figure 13f). Mean MPF was 15% for DMS images and 13% for Sentinel-2. The majority of the data fall within 0-25% MPF for both DMS imagery (100% of MPF values), and Sentinel-2 imagery (90% of MPF values). The 10% of DMS images with derived MPF in the range 25-

60% demonstrates the ability of high resolution imagery to capture more variability in the ice cover at a smaller scale, that is not fully captured by the lower-resolution (10 m) Sentinel-2 images.

Finally, we also consider images with very high MPF, inspecting those with MPF greater than 40% (821 images, 4.8% of the processed images). An example is shown of sea ice in the Lincoln Sea (Figure 13d), where a large pond in the upper left of the image had not yet drained through the thick, multiyear ice and had spread laterally across the relatively undeformed sea ice surface until a ridge was encountered. Previous studies have found MPFs of up to 75% on first year ice (Scharien & Yackel, 2005). In our study, less than 1% of images have MPFs of 75% or greater. Images with many small areas of submerged ice (ice draft) misclassified as MPs could also result in MPFs that are biased high (see Section 3.3.5, Section 5.2).

## **5 Discussion**

### **5.1 Regional Variability**

The divergence in the 2016 and 2017 results is not a function of time, but rather is related to the latitudinal location and ice types in the sampled areas. Compared to previous years, 2016 exhibited a lower sea ice extent the B/C Seas. On July 13, just prior to the commencement of the campaign, the Deadhorse meteorological station in Prudhoe Bay, Alaska experienced a record-setting high temperature of 29°C (Menne et al., 2012). The melt onset in the southern Beaufort Sea occurred in late April and early May, 6 weeks prior to the average melt onset date (Anderson et al., 2019). In contrast, the 2017 surveys were conducted north of Greenland and Ellesmere Island in the CA region, an area which experiences ice convergence as the Transpolar Drift pushes ice against the continent. Here, thick, deformed ice is trapped, and more likely to survive the summer melt season and continue to grow in the winter. Thus, the CA region is comprised of predominantly multiyear ice. These conditions result in a consolidated ice cover, with minimal open water for new ice to form. These regional differences in ice type explain the distributions of 2016 and 2017 MPF and SIC (Figures 12 and 13).

SIC in the B/C Seas region was significantly lower than in the CA (Figures 12e and f), because the ice edge retreats off the north coast of Alaska early in the melt season. The 2016 flights sampled a mix of ice types primarily in the MIZ, and a mean SIC of 69% was recorded in the B/C Seas, compared to an average SIC of 90% in the CA. The SIC distribution in the B/C Seas is bimodal due to one flight occurring in the consolidated ice pack, and the others occurring in the MIZ. The sea ice in the B/C Seas region is more mobile because it is influenced by the Beaufort Gyre, creating divergence in some areas and convergence in others. For these reasons, the standard deviation of SIC in B/C Seas region was 32%, 17% greater than that in the CA (at 15%).

The results validate the expectation that MPs present differently on the first year ice than on multiyear ice (Figure 13e). The predominantly first year ice area surveyed in 2016 exhibits a higher MPF, with more variability, than the predominantly multiyear ice area surveyed in 2017. The average MPF calculated per image in the B/C Seas is 25% with a standard deviation of 15% (Table 2). This compares with an average MPF of 14% with a standard deviation of 6% in the CA. The B/C Seas region, although predominantly first year ice, does include multiyear floes imported into the region via the Beaufort Gyre, which may explain the wider distribution of MPF in this region.

Our results also demonstrate that the MP color distribution is closely linked with ice type, as expected. Overall dark MPs dominated in the B/C Seas regions (with an average  $PCF_D$  of 60%) while light ponds dominated the CA region (with an average  $PCF_L$  of 68%). Because the color of the MP determines the amount of sunlight absorbed by the sea ice cover, our findings suggest that sunlight absorption in the Arctic is regionally variable, with lower transmission rates in the central Arctic. We can expect an increase in light transmission as the sea ice continues to transition to a higher fractional first year ice cover, although the precise nature of future changes will also be influenced by the latitudinal location of the remaining summer sea ice and its cumulative exposure to incoming solar radiation throughout the melt season. This would have important consequences for the marine ecology of the region, where large phytoplankton blooms are expected to become more common with increasing light transmission through the sea ice (Arrigo et al., 2012; Horvat et al., 2017).

## 5.2 Impact of Pixel Misclassifications on Products

Here we discuss the impact of potential pixel misclassifications (described in Section 3.3.5) on the derived products (SIC and MPF). First, we consider SIC. Pixels misclassified under case 2 and 4 (Section 3.3.5) could potentially increase SIC anomalously, while cases 1, 3, and 5 do not impact SIC. However, the overall consistency between the DMS SIC results and the independent and coincident AMSR2 and CDR SIC products (Section 4.2, Figures 12a and b), demonstrates the robustness of the pixel classification technique and the reliability of the DMS SIC. In both regions, the distributions of the DMS, AMSR2, and CDR SIC have a modal value of 95-100% SIC. Moreover, the DMS SIC product shows consistent spatial gradients in SIC with the AMSR2 SIC at a regional level as well (Figures 12a and b). Taken together, these results suggest that the pixel misclassifications contributing to a positive SIC bias are minor, and we can discount the impact of any potential misclassification on the derived SIC results.

Next we consider the impact of pixel misclassification on MPF. The misclassification of ice and open water pixels as melt pond pixels (as in cases 1-4, Section 3.3.5), could increase MPF anomalously, while misclassifications under case 5 could decrease MPF. Cases 2-4 occur most frequently in images with low SIC. To mitigate the impact of these misclassifications, we limit the MPF calculation to images with  $SIC \geq 15\%$ . However, care must be taken when interpreting results with anomalous  $MPF > 40\%$ , which although feasible (Figure 13d), may be indicative of a positive bias due to pixel misclassification.  $MPF > 40\%$  is found in 821 images, (5% of processed images), 585 of which occur in the surveys on 13 July, 2016 and 15 July, 2016 (see survey regions marked by the symbol: \*, Figure 13a).

## 6 Summary and Conclusions

Using high-resolution OIB imagery we conducted a detailed assessment of the summer sea ice cover of the Arctic Ocean. Surveys of two distinct regions allowed for the comparison of MP conditions with respect to ice type. A 2016 survey focused on the MIZ of the B/C Seas and comprised

predominantly first year ice, while in 2017 data over the consolidated multiyear ice of the CA region were collected. We described an automated, pixel-based algorithm that effectively classifies summer sea ice features in the 0.1 m-resolution DMS imagery, including undeformed sea ice, deformed sea ice, MPs and open water. Applying the algorithm to ~17,000 images, covering ~4,000 km<sup>2</sup>, we derived SIC, MPF and PCF and analyzed regional variability between the two survey sites. To our knowledge, the combined 2016 and 2017 data set provides the most widespread airborne survey of summer sea ice conditions to date.

Average SIC in the B/C Seas was 69%, 21% lower than in the CA region where an average SIC of 90% was recorded (Table 2). Ice concentration derived from the DMS imagery was, on average, 11% lower than that reported in coincident AMSR2 and CDR satellite SIC products. This is because the high-resolution DMS data allow small areas of open water to be resolved, unlike the lower-resolution, satellite-derived products where pixel averages are at km-scales. There were large regional differences in MPF between the two survey sites. We found average MPFs of 25% and 14%, in the B/C Seas and CA regions, respectively (Table 2). A wider range of MPFs, from 7% (5<sup>th</sup> percentile) to 51% (95<sup>th</sup> percentile), with a standard deviation of 15%, occurred in the B/C Seas than in the CA, where MPF ranged from 6% (5<sup>th</sup> percentile) to 22% (95<sup>th</sup> percentile), with a standard deviation of 6%. These regional differences in MPF are related to the distinct ice type at the survey site and our results conclusively show that MPF is greater on first year ice than on multiyear ice. Pond color is also dependent on the ice type on which ponds form, since pond color is related to the thickness of the underlying ice. In the B/C Seas dark ponds dominated, with a PCF of 60%, compared to a PCF of 9% and 31%, for medium and light ponds, respectively. The opposite was true in the CA region, where light ponds dominated. There, PCF of light ponds was 68%, compared with a PCF of 16% for both medium and dark ponds.

Our results have important implications for the study of Arctic-wide albedo in summer. Since 1985 the summer ice cover has transitioned from a predominantly multiyear ice cover to a seasonal ice cover (Comiso, 2012). The first year ice comprised 55% of the ice cover in the mid 1980s, compared to 77% in 2018 (Richter-Menge et al., 2019). The higher overall MPF and prevalence of dark MPs on

first year ice allows for more absorption of incoming solar radiation. Pond albedo typically ranges from 0.1 to 0.3 for dark ponds and 0.35 - 0.55 for light ponds (Perovich et al., 2002a). Our results show ponds are darker and more widespread in the B/C Seas consisting of predominantly first year ice. We therefore expect changes in pond fraction and color to accompany changes in ice type. This, in conjunction with a diminishing ice extent, would exacerbate the ice-albedo feedback, increasing Arctic-wide solar absorption. Additionally, MPs create a weaker ice pack, making the ice more vulnerable to break up in Arctic storms, such as occurred in 2012 (Parkinson & Comiso, 2016). The precise nature of future changes will also be influenced by the latitudinal location of the remaining summer sea ice.

The novel dataset derived in this study consists of seven binary masked arrays per image for each classification type: border, undeformed ice, deformed ice, open water, and light, medium, and dark MPs. The MPF, SIC, and PCF parameters are available per image. These data are of keen interest to the community for a number of related studies. Sea ice modelers may find these parameters useful for understanding MP shapes and fractions in initialization and validation of models. The MP shapes and areas (see Figure 9b and c), can provide information on transmission of light through the ice pack (Light et al., 2015) for those who study under ice ecology. The MPF product can be used to validate satellite MP products, e.g. the MODIS MPF as described in Rösel and Kaleschke, 2012. Similarly, the SIC product could be used for validation of the AMSR2 and CDR SIC (Meier et al., 2018, Meier et al., 2017a).

Our classification algorithm is designed to automatically adjust to overhead lighting conditions and can be applied to other, high-resolution, natural-color RGB imagery such as the 10 m-resolution Sentinel-2 Multispectral Instrument satellite measurements, the airborne CAMBOT imagery captured during the OIB August 2019 summer campaign, and available WorldView multi-spectral satellite imagery (0.3 m maximum resolution). With the possibility of analyzing datasets that span multiple years and various regions, there is potential to investigate MPF variability and trends with time.

The DMS-derived data products may also be used in conjunction with high-resolution laser altimetry. During the OIB summer campaigns, the Airborne Topographic Mapper (ATM), a conically

Accepted Article

scanning laser altimeter, was operated in conjunction with DMS. The ATM laser waveform return consists of surface and bottom-of-pond reflections, from which pond depth can be derived. Pond depth, in conjunction with the DMS MP mask derived here, provides an estimate of MP volume, which is important for calculating freshwater fluxes in summer (Zhang et al., 2018). Knowledge of the distribution and coverage of MPs on Arctic sea ice presented here will inform interpretation of altimeter data collected by OIB and ICESat-2 in summer 2019, and can be used to understand future laser altimeter surveys of summer sea ice conditions in the Arctic.

## Acknowledgments and Data

This study is supported under the NASA Cryosphere Program Grant 80NSSC17K0006. We thank the DMS instrument team and the OIB science team for collecting and processing the data used in this study. The IceBridge DMS L1B Geolocated and Orthorectified Images, Version 1 data are available at <http://dx.doi.org/10.5067/OZ6VNOPMPRJ0>. The NOAA/NSIDC Climate Data Record of Passive Microwave Sea Ice Concentration, Version 3 is available at <https://doi.org/10.7265/N59P2ZTG>. The AMSR-E/AMSR2 Unified L3 Daily 12.5 km Brightness Temperatures, Sea Ice Concentration, Motion & Snow Depth Polar Grids, Version 1 data are available at: <https://doi.org/10.5067/RA1MIJOYPK3P>. The summer melt data products derived in this study are available at the NOAA Laboratory for Satellite Altimetry

(<ftp://ftp.star.nesdis.noaa.gov/pub/socd/lisa/SeaIceProducts/Airborne/IceBridge/SummerMelt/>) The contents of this manuscript are solely the work product of the authors and should not be construed as a statement of policy or position of NOAA or the U.S. Government.

## References

- Anderson, M., Bliss, A. C., & Drobot, S. (2019). *Snow Melt Onset Over Arctic Sea Ice from SMMR SSM/I-SSMIS Brightness Temperatures, Version 4*. Boulder, Colorado, USA. NASA National Snow and Ice Data Center Distributed Active Archive Center. <https://doi.org/10.5067/A9YK15H5EBHK>. [24 Sept, 2019].
- Arrigo K. R., Perovich D. K., Pickart R. S., Brown Z. W., Van Dijken G. L., Lowry K. E., et al. (2012). Massive phytoplankton blooms under arctic sea ice, *Science*, 336 (6087), 1408-1408. <https://doi.org/10.1126/science.1215065>.
- Boisvert, L. N., Markus, T., & Vihma, T. (2013). Moisture flux changes and trends for the entire Arctic in 2003-2011 derived from EOS Aqua data. *J. Geophys. Res.*, 118, 5829–5843. <https://doi.org/10.1002/jgrc.20414>.
- Comiso, J. C. (2012). Large Decadal Decline of the Arctic Multiyear Ice Cover. *J. Climate*, 25, 1176–1193. <https://doi.org/10.1175/JCLI-D-11-00113.1>.
- Comiso, J. C., Parkinson, C.L., Gersten, R., & Stock, L. (2008). Accelerated decline in the Arctic sea ice cover. *Geophys. Res. Lett.*, 35, 1–6. <https://doi.org/10.1029/2007GL031972>.
- Curry, J. A., Schramm, J. L., Perovich, D.K., & Pinto, J.O. (2001). Applications of SHEBA/FIRE data to evaluation of snow/ice albedo parameterizations. *J. Geophys. Res. Atmos.*, 106, 15345–15355. <https://doi.org/10.1029/2000JD900311>.
- Curry, J. A., Schramm, J. L., & Ebert, E. E. (1995). Sea Ice-Albedo Climate Feedback Mechanism. *J. Clim.*, 8, 240–247. [https://doi.org/10.1175/1520-0442\(1995\)008<0240:SIACFM>2.0.CO;2](https://doi.org/10.1175/1520-0442(1995)008<0240:SIACFM>2.0.CO;2).
- Dominguez, R. (2010, updated 2018). IceBridge DMS L1B Geolocated and Orthorectified Images, Version 1. Boulder, Color. USA. NASA Natl. Snow Ice Data Cent. Distrib. Act. Arch. Cent. <https://doi.org/10.5067/OZ6VNOPMPRJ0>. [18 January, 2018].
- Duncan, K., Farrell, S.L., Connor, L.N., Richter-Menge, J., Hutchings, J.K., & Dominguez, R. (2018). High-resolution airborne observations of sea-ice pressure ridge sail height. *Ann. Glaciol.*, 59, 137–147. <https://doi.org/10.1017/aog.2018.2>.
- Eicken, H., Grenfell, T.C., Perovich, D.K., Richter-Menge, J.A. & Frey, K. (2004). Hydraulic controls of summer Arctic pack ice albedo. *J. Geophys. Res.*, 109, 1–13. <https://doi.org/10.1029/2003JC001989>
- Farrell, S. L., Markus, T., Kwok, R., & Connor, L. (2011). Laser altimetry sampling strategies over sea ice. *Ann. Glaciol.*, 52, 69–76. <https://doi.org/10.3189/172756411795931660>.
- Fetterer, F., & Untersteiner, N. (1998). Observations of melt ponds on Arctic sea ice. *J. Geophys. Res. Ocean.*, 103, 24821–24835. <https://doi.org/10.1029/98JC02034>.
- Flocco, D., Feltham, D. L., & Turner, A. K. (2010). Incorporation of a physically based melt pond scheme into the sea ice component of a climate model. *J. Geophys. Res.*, 115, C08012. <https://doi.org/10.1029/2009JC005568>.
- Flocco, D., Schröder, D., Feltham, D. L., & Hunke, E. C. (2012). Impact of melt ponds on Arctic sea ice simulations from 1990 to 2007. *J. Geophys. Res.*, 117, C09032. <https://doi.org/10.1029/2012JC008195>.

Haas, C. (2017). Sea ice thickness distribution. In *Sea Ice*, David N. Thomas (Eds.), John Wiley & Sons, Ltd. (p 42-64), 652 pp. .

Horvat, C., Jones, D. R., Iams, S., Schroeder, D., Flocco, D., & Feltham, D. (2017). The frequency and extent of sub-ice phytoplankton blooms in the Arctic Ocean. *Science advances*, 3(3), e1601191.

Hunke, E. C., Lipscomb, W.H., & Turner, A.K. (2010), Sea-ice models for climate study: retrospective and new directions. *J. Glaciol.*, 56, 1162–1172.

<https://doi.org/10.3189/002214311796406095>.

Istomina, L., Heygster, G., Huntemann, M., Schwarz, P., Birnbaum, G., Scharien, R., et al. (2015). Melt pond fraction and spectral sea ice albedo retrieval from MERIS data - Part 1: Validation against in situ, aerial, and ship cruise data. *The Cryosphere*, 9, 1551–1566.  
<https://doi.org/10.5194/tc-9-1551-2015>.

Koenig, L. S., Martin, S., Stundinger, M., & Sonntag, J. (2010). Polar Airborne Observations Fill Gap in Satellite Data. *EOS*, 91, 333-334. <https://doi.org/10.1029/2010EO380002>

Krabill, W. B., Abdalati, W., Frederick, E. B., Manizade, S. S., Martin, C. F., Sonntag, J. G., et al. (2002). Aircraft laser altimetry measurement of elevation changes of the Greenland ice sheet: Technique and accuracy assessment. *J. Geodynamics*, 34 (3/4), 357–376.  
[https://doi.org/10.1016/S0264-3707\(02\)00040-6](https://doi.org/10.1016/S0264-3707(02)00040-6)

Kwok, R. (2015). Sea ice convergence along the Arctic coasts of Greenland and the Canadian Arctic Archipelago: Variability and extremes (1992-2014). *Geophys. Res. Lett.*, 42, 7598–7605.  
<https://doi.org/10.1002/2015GL065462>.

Light, B., Perovich, D. K., Webster, M. A., Polashenski, C., and Dadic, R. (2015). Optical properties of melting first-year Arctic sea ice. *J. Geophys. Res. Oceans*, 120, 7657-7675.  
<https://doi.org/10.1002/2015JC011163>.

Lu, P., Leppäranta, M., Cheng, B., Li, Z., Istomina, L., & Heygster, G. (2018). The color of melt ponds on Arctic sea ice. *The Cryosphere*, 12, 1331–1345. <https://doi.org/10.5194/tc-12-1331-2018>.

Lüthje, M., Feltham, D. L., Taylor, P. D., & Worster M. G. (2006). Modeling the summertime evolution of sea-ice melt ponds. *J. Geophys. Res.*, 111, C02001.  
<http://doi.org/10.1029/2004JC002818>

Mäkynen, M., Kern, S., Rösel, A., & Pedersen, L. T. (2014). On the estimation of melt pond fraction on the arctic sea ice with ENVISAT WSM images. *IEEE Trans. Geosci. Remote Sens.*, 52, 7366–7379. <https://doi.org/10.1109/TGRS.2014.2311476>.

Markus, T., Cavalieri, D. J., & Ivanoff, A. (2002). The potential of using Landsat 7 ETM+ for the classification of sea-ice surface conditions during summer. *Ann. Glaciol.*, 34, 415–419.  
<https://doi.org/10.3189/172756402781817536>.

Markus, T., Cavalieri, D.J., Tschudi, M.A., & Ivanoff, A. (2003). Comparison of aerial video and Landsat 7 data over ponded sea ice. *Remote Sens. Environ.*, 86, 458–469.  
[https://doi.org/10.1016/S0034-4257\(03\)00124-X](https://doi.org/10.1016/S0034-4257(03)00124-X).

Meier, W. N., Fetterer, F., Savoie, M., Mallory, S., Duerr, R., & Stroeve, J. (2017a). *NOAA/NSIDC Climate Data Record of Passive Microwave Sea Ice Concentration, Version 3*. Boulder, Colorado

- USA. NSIDC: National Snow and Ice Data Center. <https://doi.org/10.7265/N59P2ZTG>. [8, May 2019].
- Meier, W. N., Stewart, J. S., Liu, Y., Key, J., & Miller, J. A. (2017b). Operational Implementation of Sea Ice Concentration Estimates from the AMSR2 Sensor. *IEEE Journal of Selected Topics in Applied Earth Observations and Remote Sensing*, 10(9), 3904-3911. <https://doi.org/10.1109/jstars.2017.2693120>
- Meier, W. N., Markus, T., & Comiso, J. C. (2018). *AMSR-E/AMSR2 Unified L3 Daily 12.5 km Brightness Temperatures, Sea Ice Concentration, Motion & Snow Depth Polar Grids, Version 1*. Boulder, Colorado USA. NASA National Snow and Ice Data Center Distributed Active Archive Center. <https://doi.org/10.5067/RA1MIJOYPK3P>. [8 May, 2019].
- Menne, M. J., Durre, I., Korzeniewski, B., McNeal, S., Thomas, K., Yin, X., et al. (2012, updated daily). Global Historical Climatology Network - Daily [GHCN-Daily], Version 3. <https://doi.org/10.7289/V5D21VHZ> [29 Sept 2019]
- Miao, X., Xie, H., Ackley, S. F., Perovich, D. K., & Ke, C. (2015). Object-based detection of Arctic sea ice and melt ponds using high spatial resolution aerial photographs. *Cold Reg. Sci. Technol.*, 119, 211–222. <https://doi.org/10.1016/j.coldregions.2015.06.014>.
- Newman, T., Farrell, S. L., Richter-Menge, J., Connor, L. N., Kurtz, N. T., Elder, B. C., & McAdoo, D. (2014). Assessment of radar-derived snow depth over Arctic sea ice. *J. Geophys. Res. Ocean.*, 119, 8578–8602. <https://doi.org/10.1002/2014JC010284>.
- Onana, V. D. P., Kurtz, N. T., Farrell, S. L., Koenig, L. S., Studinger, M., & Harbeck, J. P. (2013). A Sea-Ice Lead Detection Algorithm for Use with High-Resolution Airborne Visible Imagery. *IEEE Trans. Geosci. Remote Sens.*, 51, 38–56. <https://doi.org/10.1109/TGRS.2012.2202666>.
- Parkinson, C. L., & Comiso, J. C. (2016). On the 2012 record low Arctic sea ice cover: Combined impact of preconditioning and an August storm. *Geophys. Res. Lett.*, 40, 1356-1361. <https://doi.org/10.1002/grl.50349>.
- Perovich, D. K. (2017). Sea ice and sunlight, in *Sea Ice*, David N. Thomas (Eds.), John Wiley & Sons Ltd., 110-137, 652 pp.
- Perovich, D. K., Grenfell, T.C., Light, B., & Hobbs, P.V. (2002a). Seasonal evolution of the albedo of multiyear Arctic sea ice. *J. Geophys. Res.*, 107, 8044. <https://doi.org/10.1029/2000JC000438>.
- Perovich, D. K., & Polashenski, C. (2012). Albedo evolution of seasonal Arctic sea ice. *Geophysical Research Letters*, 39(8). <https://doi.org/10.1029/2012GL051432>
- Perovich, D. K., Roesler, C. S., & Pegau, W. S. (1998). Variability in Arctic sea ice optical properties. *Journal of Geophysical Research: Oceans*, 103(C1), 1193-1208. <https://doi.org/10.1029/97JC01614>
- Perovich, D. K., Tucker III, W. B. , & Ligett, K. A. (2002b). Aerial observations of the evolution of ice surface conditions during summer. *J. Geophys. Res.*, 107, 8048. <https://doi.org/10.1029/2000JC000449>.
- Petrich, C., Eicken, H., Polashenski, C. M. , Sturm, M., Harbeck, J. P., Perovich, D. K., & Finnegan, D. C. (2012). Snow dunes: A controlling factor of melt pond distribution on Arctic sea ice. *J. Geophys. Res.*, 117, C09029 <https://doi.org/10.1029/2012JC008192>.
- Richter-Menge, J., & Farrell, S. L. (2013). Arctic Sea Ice Conditions in Spring 2009 - 2013 Prior to Melt. *Geophys. Res. Lett.*, 40, 5888-5893. <https://doi.org/10.1002/2013GL058011>.

- Richter-Menge, J., Osborne, E., Druckenmiller, M., Jeffries, M. O., Eds., 2019: The Arctic [in “State of the Climate in 2018”]. *Bull. Amer. Meteor. Soc.*, 100 (9), S141–S168.  
<https://doi.org/10.1175/2019BAMSStateoftheClimate.1>.
- Rösel, A., Kaleschke, L., & Birnbaum, G. (2012). Melt ponds on Arctic sea ice determined from MODIS satellite data using an artificial neural network. *The Cryosphere*, 6, 431–446.  
<https://doi.org/10.5194/tc-6-431-2012>.
- Rösel, A., & Kaleschke, L. (2011). Comparison of different retrieval techniques for melt ponds on Arctic sea ice from Landsat and MODIS satellite data. *Ann. Glaciol.*, 52, 185–191.  
<https://doi.org/10.3189/172756411795931606>.
- Rösel, A., & Kaleschke, L. (2012). Exceptional melt pond occurrence in the years 2007 and 2011 on the Arctic sea ice revealed from MODIS satellite data. *J. Geophys. Res. Ocean.*, 117, 1–9.  
<https://doi.org/10.1029/2011JC007869>.
- Sallila, H., Farrell, S. L., McCurry, J., and Rinne, E. (2019). Assessment of Contemporary Satellite Sea Ice Thickness Products for Arctic Sea Ice. *The Cryosphere*, 13, 1187–1213.  
<https://doi.org/10.5194/tc-13-1187-2019>.
- Scharien, R. K., & Yackel, J. J. (2005). Analysis of surface roughness and morphology of first-year sea ice melt ponds: Implications for microwave scattering. *IEEE Transactions on Geoscience and Remote Sensing*, 43(12), 2927–2939. <https://doi.org/10.1109/TGRS.2005.857896>.
- Schröder, D., Feltham, D. L., Flocco, D., & Tsamados, M. (2014). September Arctic sea-ice minimum predicted by spring melt-pond fraction. *Nat. Clim. Chang.*, 4, 353–357.  
<https://doi.org/10.1038/nclimate2203>.
- Skyllingstad, E. D., Paulson, C. A., & Perovich, D. K. (2009). Simulation of melt pond evolution on level ice. *J. Geophys. Res.*, 114, C12019. <https://doi.org/10.1029/2009JC005363>.
- Steele, M., Zhang, J., & Ermold, W. (2010). Mechanisms of summertime upper Arctic Ocean warming and the effect on sea ice melt. *J. Geophys. Res.*, 115, C11004.  
<https://doi.org/10.1029/2009JC005849>
- Tschudi, M. A., Curry, J. A., & Maslanik, J. A. (2001). Airborne observations of summertime surface features and their effect on surface albedo during FIRE/SHEBA. *J. Geophys. Res. Atmos.*, 106, 15335–15344. <https://doi.org/10.1029/2000JD900275>
- Tschudi, M. A., Maslanik, J.A., & Perovich, D.K. (2008). Derivation of melt pond coverage on Arctic sea ice using MODIS observations. *Remote Sens. Environ.*, 112, 2605–2614.  
<https://doi.org/10.1016/j.rse.2007.12.009>.
- Tsamados, M., Feltham, D., Petty, A., Schroeder, D., & Flocco, D. (2015). Processes controlling surface, bottom and lateral melt of Arctic sea ice in a state of the art sea ice model. *Philosophical Transactions of the Royal Society A: Mathematical, Physical and Engineering Sciences*, 373(2052). <https://doi.org/10.1098/rsta.2014.0167>.
- Uttal, T., Curry, J. A., Mcphee, M., Perovich, D. K., Moritz, R., Maslanik, J. A., et al. (2002). Surface Heat Budget of the Arctic Ocean. *Bull. Am. Meteorol. Soc.*, 83, 255–275.  
[https://doi.org/10.1175/1520-0477\(2002\)083<0255:shbota>2.3.co;2](https://doi.org/10.1175/1520-0477(2002)083<0255:shbota>2.3.co;2).
- Webster, M.A., Rigor, I.G., Perovich, D.K., Richter-Menge, J.A., Polashenski, C.M. & Light, B. (2015). Seasonal evolution of melt ponds on Arctic sea ice. *J. Geophys. Res.*, 120, 1–15.  
<https://doi.org/10.1002/2015JC011030>.

World Meteorological Organization (WMO) (1970). Sea ice nomenclature. Terminology, codes and illustrated glossary. No. 259, Geneva, Switzerland.

Wright, N. C., & Polashenski, C. M. (2018). Open-source algorithm for detecting sea ice surface features in high-resolution optical imagery. *The Cryosphere*, 12, 1307–1329. <https://doi.org/10.5194/tc-12-1307-2018>.

Yan, J.-B., S. Gogineni, F. Rodriguez-Morales, D. Gomez-Garcia, J. Paden, J. Li, C. Leuschen, D. Braaten, J. Richter-Menge, S. Farrell, J. Brozena and R. Hale (2017). Airborne Measurements of Snow Thickness: Using ultrawide-band frequency-modulated-continuous-wave radars, *IEEE Geosci. Rem. Sens. Mag.*, 5(2), 57-76. <https://doi.org/10.1109/MGRS.2017.2663325>

Zege, E., Malinka, A., Katsev, I., Prikhach, A., Heygster, G., Istomina, L., et al. (2015). Algorithm to retrieve the melt pond fraction and the spectral albedo of Arctic summer ice from satellite optical data. *Remote Sens. Environ.*, 163, 153–164. <https://doi.org/10.1016/j.rse.2015.03.012>.

Zhang, J., Schweiger, A., Webster, M., Light, B., Steele, M., Ashjian, C., et al. (2018). Melt pond conditions on declining Arctic sea ice over 1979-2016: Model development, validation, and results. *Journal of Geophysical Research*, 123(11), 7983-8003. <https://doi.org/10.1029/2018JC014298>

**Table 1.** Summary of data collected during OIB Arctic summer sea ice campaigns

Dates	13-21 July 2016	17-25 July 2017
Base airport	Utqiagvik (Barrow), Alaska	Thule, Greenland
Survey location	Beaufort Sea & Chukchi Sea (B/C Seas)	Lincoln Sea & central Arctic Ocean (CA)
Number of sea ice flights	6	5
Total area surveyed	~ 2940 km <sup>2</sup> (25,603 DMS images)	~ 2360 km <sup>2</sup> (20,559 DMS images)
Ice type (Haas, 2017)	Mixed first year and multiyear	Multiyear
Mean winter sea ice thickness (Haas, 2017)	1-2.5 m	3-6 m

**Table 2.** Results of automatic surface classification, averaged per flight.

Flight Date	Classification Category (%)							Sea Ice Concentration (%)					Melt Pond Fraction (%)				
	N	UI	DI	OW	DMP	MMP	LMP	N	mean	5%	95%	stdev	N	mean	5%	95%	stdev
<b>13 July 2016</b>	1759	42.9	0.2	38.4	5.1	2.5	10.9	1759	61.6	0.0	100.0	43.4	1222	31.2	12.4	67.6	16.5
<b>14 July 2016</b>	1523	61.2	0.5	18.9	10.3	2.6	6.5	1523	81.1	26.9	100.0	22.3	1475	23.2	10.6	40.8	11.5
<b>15 July 2016</b>	2540	45.6	0.6	32.2	17.2	0.8	3.6	2540	67.8	11.6	100.0	26.8	2351	31.9	17.4	61.7	14.8
<b>19 July 2016</b>	2774	54.1	0.4	31.5	9.2	1.1	3.7	2774	68.5	0.0	100.0	29.4	2469	20.0	8.9	33.8	8.0
<b>20 July 2016</b>	225	55.8	1.2	29.7	9.7	1.3	2.3	225	70.3	0.0	100.0	34.6	193	18.7	1.5	92.0	25.2
<b>21 July 2016</b>	654	60.5	1.3	26.6	7.0	1.1	3.5	654	73.4	0.0	100.0	32.9	577	16.3	1.4	55.0	17.8
<b>17 July 2017</b>	985	83.0	0.5	7.6	1.6	0.5	6.8	985	92.4	71.4	100.0	11.5	980	9.6	3.1	19.7	7.6
<b>18 July 2017</b>	158	84.6	1.0	4.2	1.1	1.1	8.0	158	95.8	86.7	100.0	4.6	158	10.6	4.7	23.5	5.9
<b>24 July 2017</b>	2268	69.8	1.0	15.9	2.2	2.8	8.3	2268	84.1	14.4	100.0	22.2	2153	15.7	9.5	22.0	5.0
<b>25 July 2017 (a)</b>	2120	79.3	0.3	6.7	3.0	2.5	8.2	2120	93.3	79.6	100.0	7.5	2119	14.6	6.5	23.4	6.0
<b>25 July 2017 (b)</b>	2027	78.5	0.0	8.9	1.2	1.4	10.0	2027	91.1	75.1	100.0	9.7	2027	13.8	7.8	19.8	4.5

Table 2 footnote: Percentage of surface pixels in classification categories: undeformed ice (UI), deformed ice (DI), open water (OW), dark melt pond (DMP), medium melt pond (MMP) and light melt pond (LMP). N is the total number of classified images per flight.

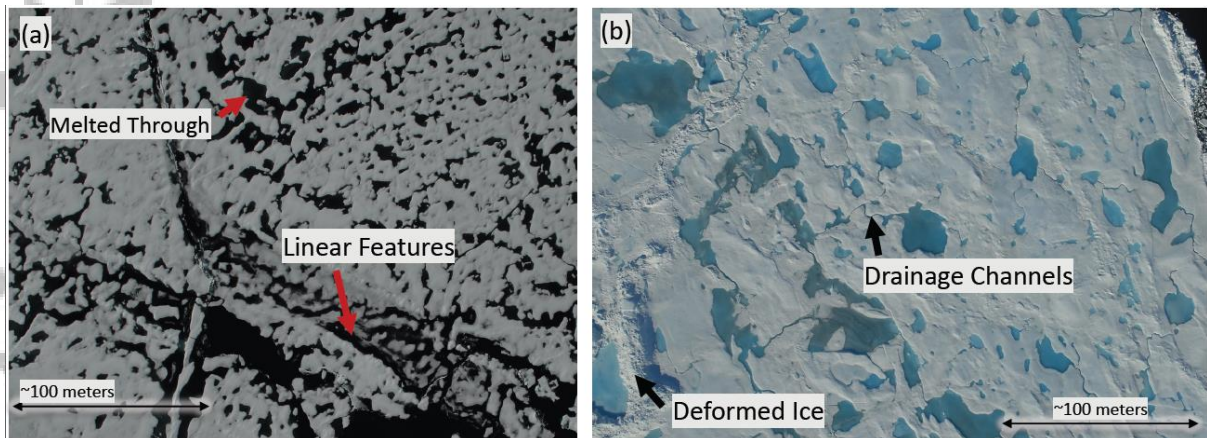


**Figure 1.** High-resolution, visible-band airborne imagery of MPs. (a) first year sea ice in the Beaufort Sea, 14 July, 2016. (b) multiyear sea ice north of Ellesmere Island, 24 July, 2017.

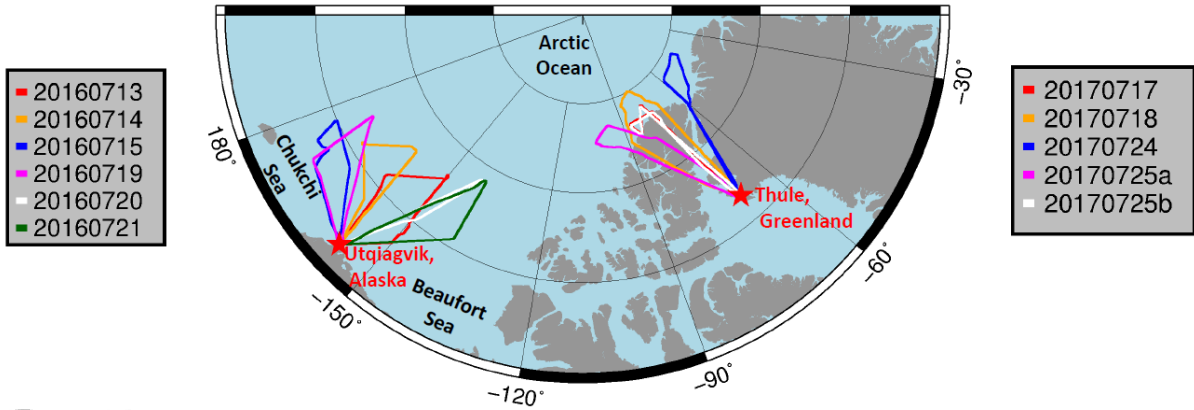


**Figure 2.** Operation IceBridge Arctic summer flight surveys over sea ice based in

Utqiagvik (Barrow), Alaska and Thule, Greenland. 2016 surveys were over the Beaufort and Chukchi Seas (B/C Seas region), 2017 surveys over the Lincoln Sea and central Arctic Ocean (CA region), north of Ellesmere Island.

Accepted Article

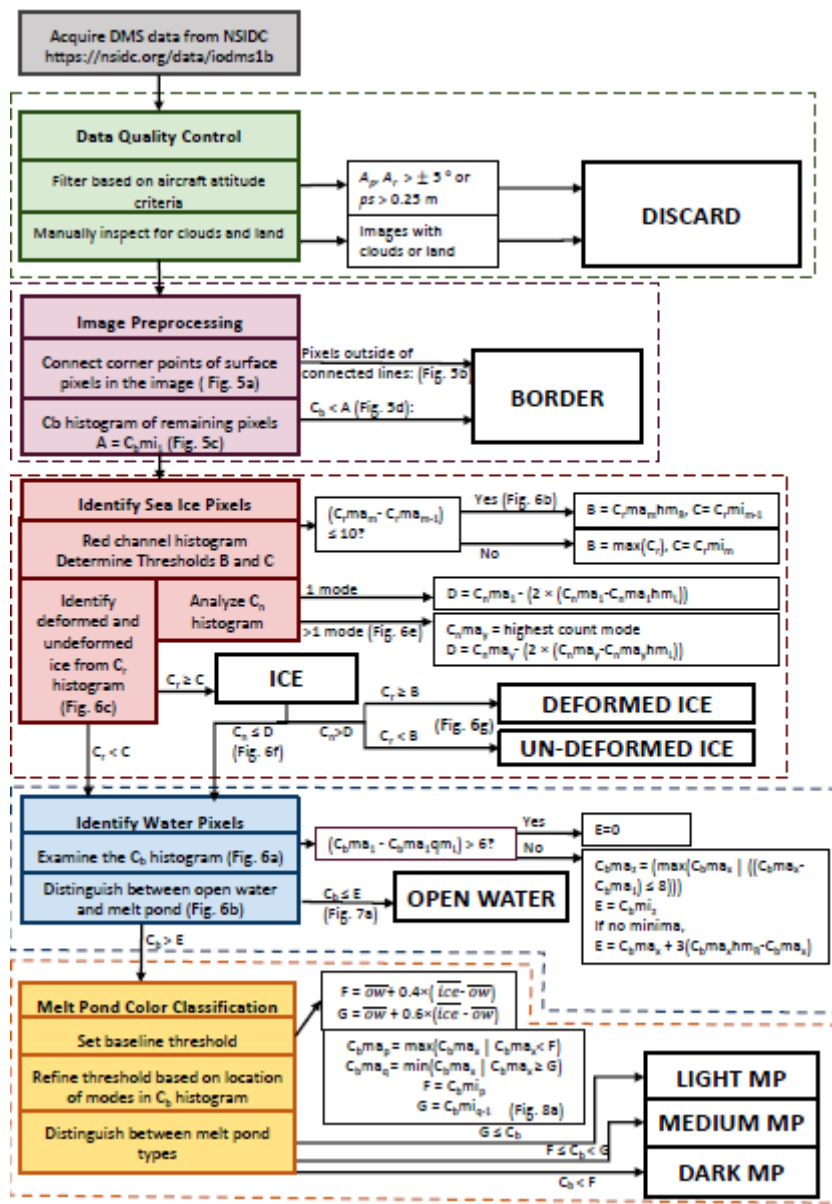


**Figure 3.** A schematic detailing the surface classification algorithm including steps to identify deformed ice, undeformed ice, open water and MP pixels. Corresponding figures are noted, where applicable. The notation “|” is used to mean “such that.” Colored boxes indicate the classification steps, with equations describing specific conditions and thresholds, including data quality control (green, see text Section 3.1), image preprocessing (purple, Section 3.2), sea ice classification (red, Section 3.3.1), open water classification (blue, Section 3.3.2), and the MP classification algorithm (gold, Section 3.3.3). Final outputs are indicated by white boxes with thick black outlines.

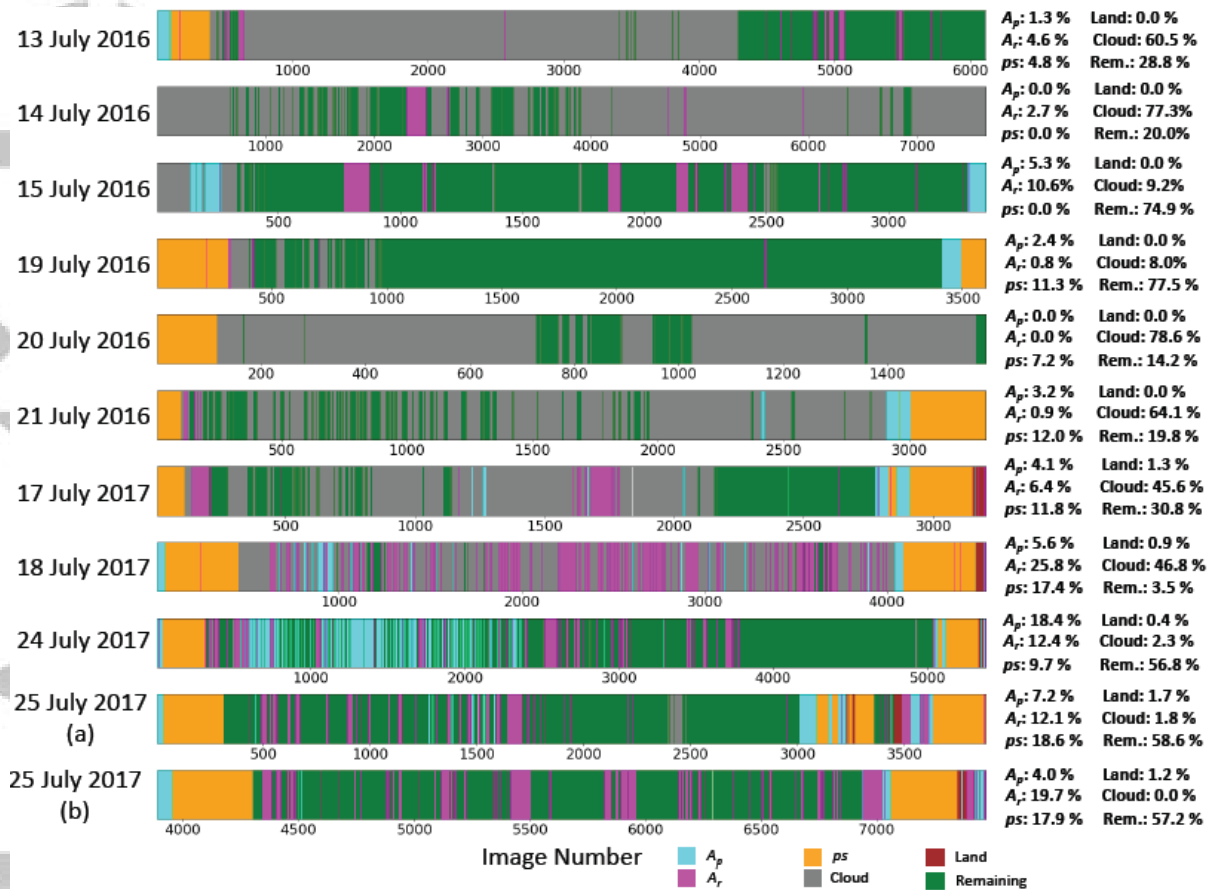


**Figure 4.** Quality control results of 11 DMS Arctic sea ice surveys. Each horizontal bar is associated with one survey. Each image is represented by a vertical line. The color of the line indicates whether the image meets the quality control criteria and continues to the preprocessing steps (green) or the reason for its removal from the data set: pitch ( $A_p$ , cyan), roll ( $A_r$ , pink), or pixel size ( $ps$ , orange) exceeded threshold, cloud contamination (gray), or land contamination (maroon). The percentage of data flagged under each quality control criteria and data remaining (green) for processing is given on the right. Rem= remaining.

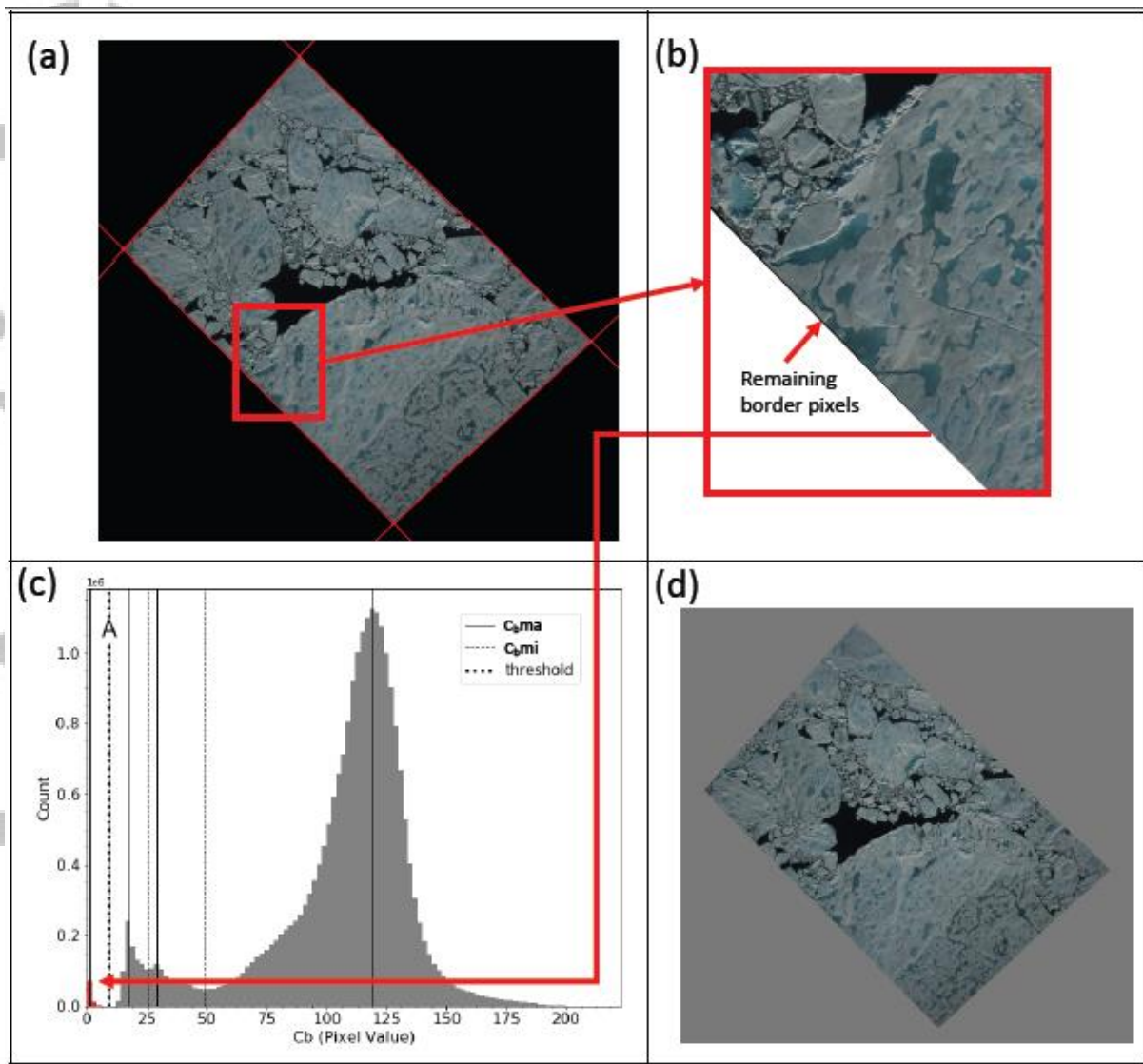


**Figure 5.** Methodology to identify DMS border pixels. (a) original GeoTIFF image of sea ice in the Lincoln Sea at  $-51.6^{\circ}\text{W}$ ,  $83.2^{\circ}\text{N}$  on 24 July, 2017, with the corner points of the surface pixel array connected (thin red lines). (b) residual border pixels remain unclassified after the first identification step. (c) distribution of  $C_b$  pixels. Residual border pixels are identified where  $C_b < C_{bmi1}$  (red). (d) same as in (a) but with all border pixels identified (gray), revealing the remaining surface pixels (natural color).

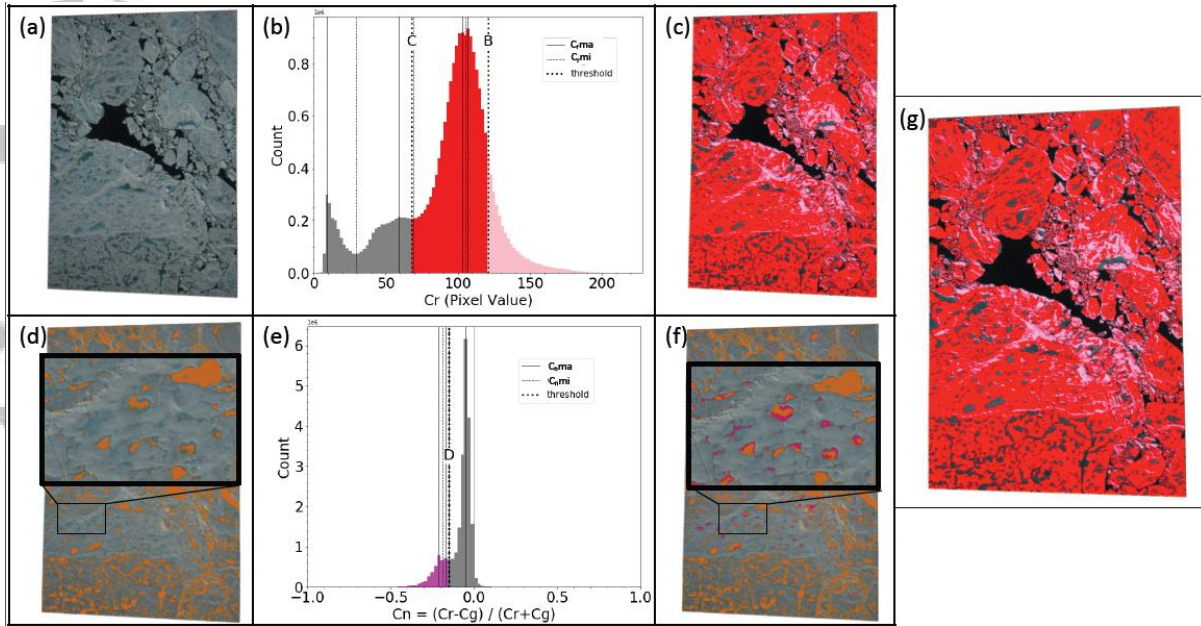


**Figure 6.** Methodology to identify ice (both undeformed and deformed) pixels. (a) surface pixels (after preprocessing). (b) distribution of surface pixels  $C_r$ , where thresholds B and C (Section 3.3.1) are identified to separate ice pixels from other surface pixels (threshold C) and deformed (pink) from undeformed ice (red) (threshold B). (c) classification of undeformed ice pixels (red), deformed ice pixels (pink), and remaining surface pixels (open water and ponded ice, natural color) after the first iteration. (d) image distinguishing between pixels classified as ice (undeformed and deformed, natural color) and surface pixels remaining (orange), demonstrating the need for a second iteration to remove misclassified pixels from the ice mask, refining the results of the first iteration. (e) distribution of normalized pixel value ( $C_n$ ) of all surface pixels. Pixels where  $C_n < D$  are shown in magenta and are not ice pixels. (f) image distinguishing pixels classified as ice (natural color), pixels not classified as ice after the first iteration (orange), and pixels misclassified as ice in the first iteration and removed from ice mask in second iteration (magenta). (g) classified image after second iteration, showing undeformed ice (red), deformed ice (pink), and unclassified pixels (natural color).

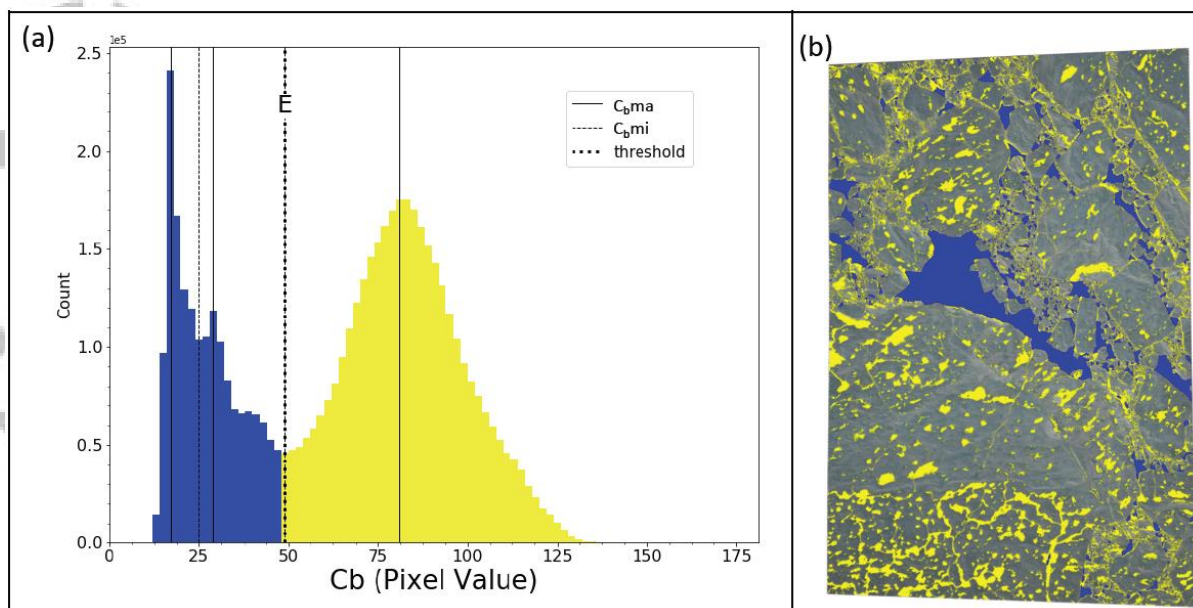


**Figure 7.** Methodology to identify open water pixels. (a) distribution of  $C_b$  pixels remaining after ice pixels have been classified. Threshold  $E$  separates open water pixels (blue) from MP pixels (yellow). (b) classified image showing open water pixels (blue), MP pixels (yellow), and ice pixels (natural color).

Accepted

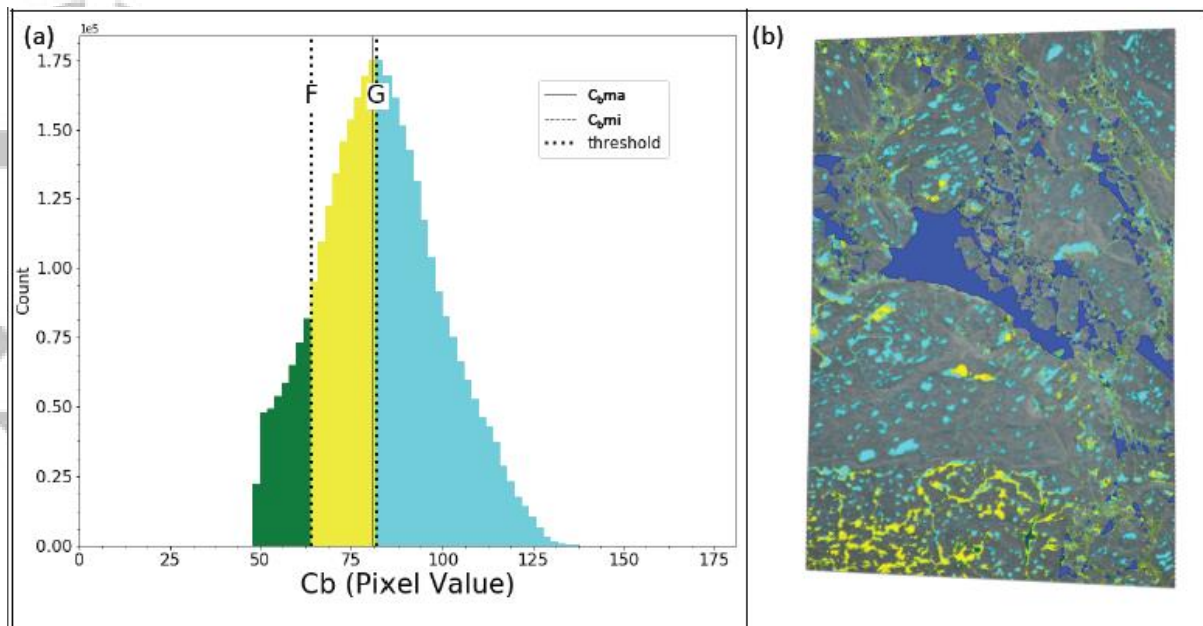


**Figure 8.** Methodology to classify MPs. (a) distribution of  $C_b$  pixels showing thresholds for cutoff between dark (green)/medium (yellow) MPs and between medium/light (cyan) MPs, F and G, respectively. (b) classified image showing open water (blue), dark (green), medium (yellow), and light (cyan) MPs, and previously classified ice pixels (natural color).

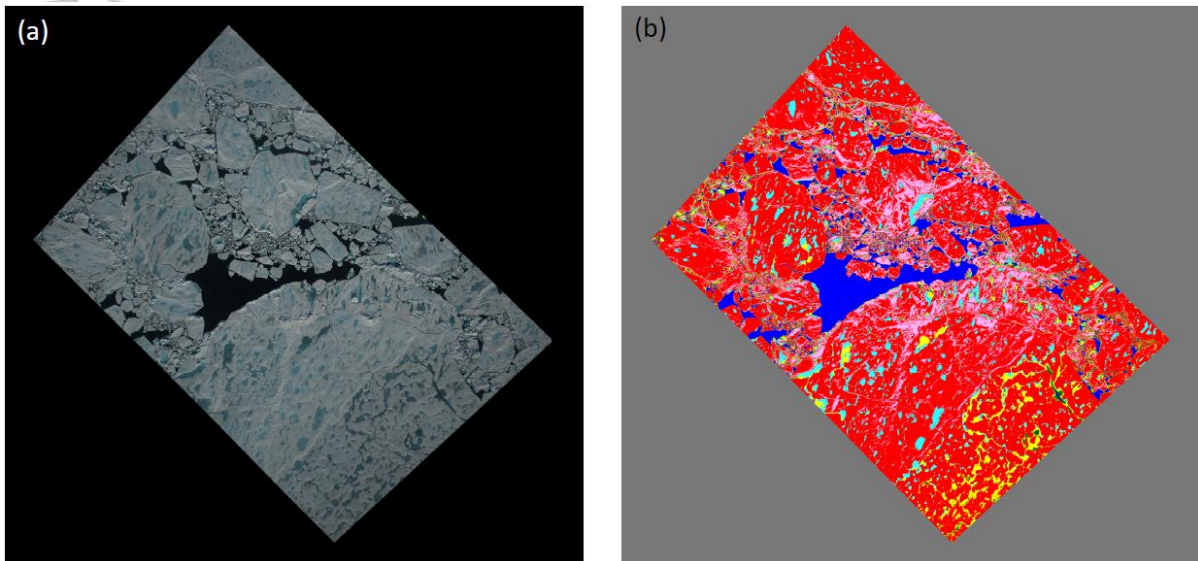


**Figure 9.** Final result of image classification algorithm. (a) original DMS GeoTIFF (same as in Figure 5a). (b) DMS image after classification showing pixels identified as border (gray), undeformed ice (red, 64%), deformed ice (pink, 13%), open water (blue, 8%), dark MPs (green, 2%), medium MPs (yellow, 5%), and light MPs (cyan, 8%).

Accepted

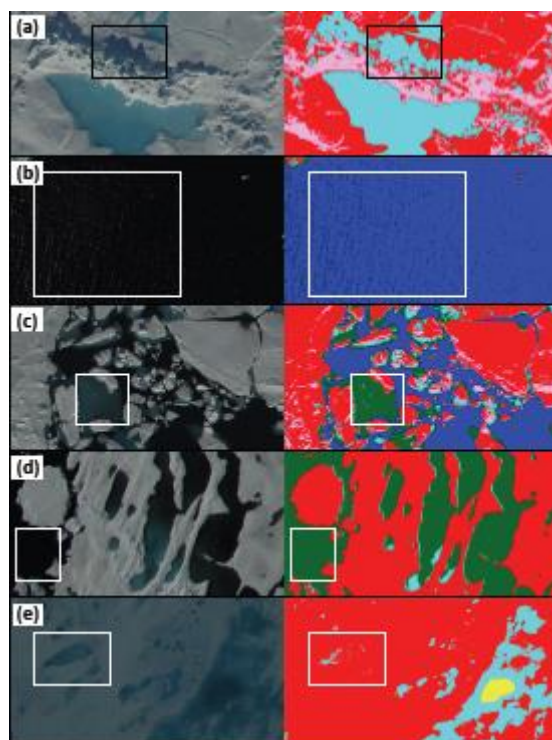


**Figure 10.** Examples of pixel misclassification. Areas with misclassified pixels are in white boxes in the zoom of original DMS GeoTIFF on the left, and classified image on the right to exemplify pixel misclassifications of: (a) ridge shadows, (b) sun glint, (c) ice draft, (d) open water, and (e) light melt ponds.

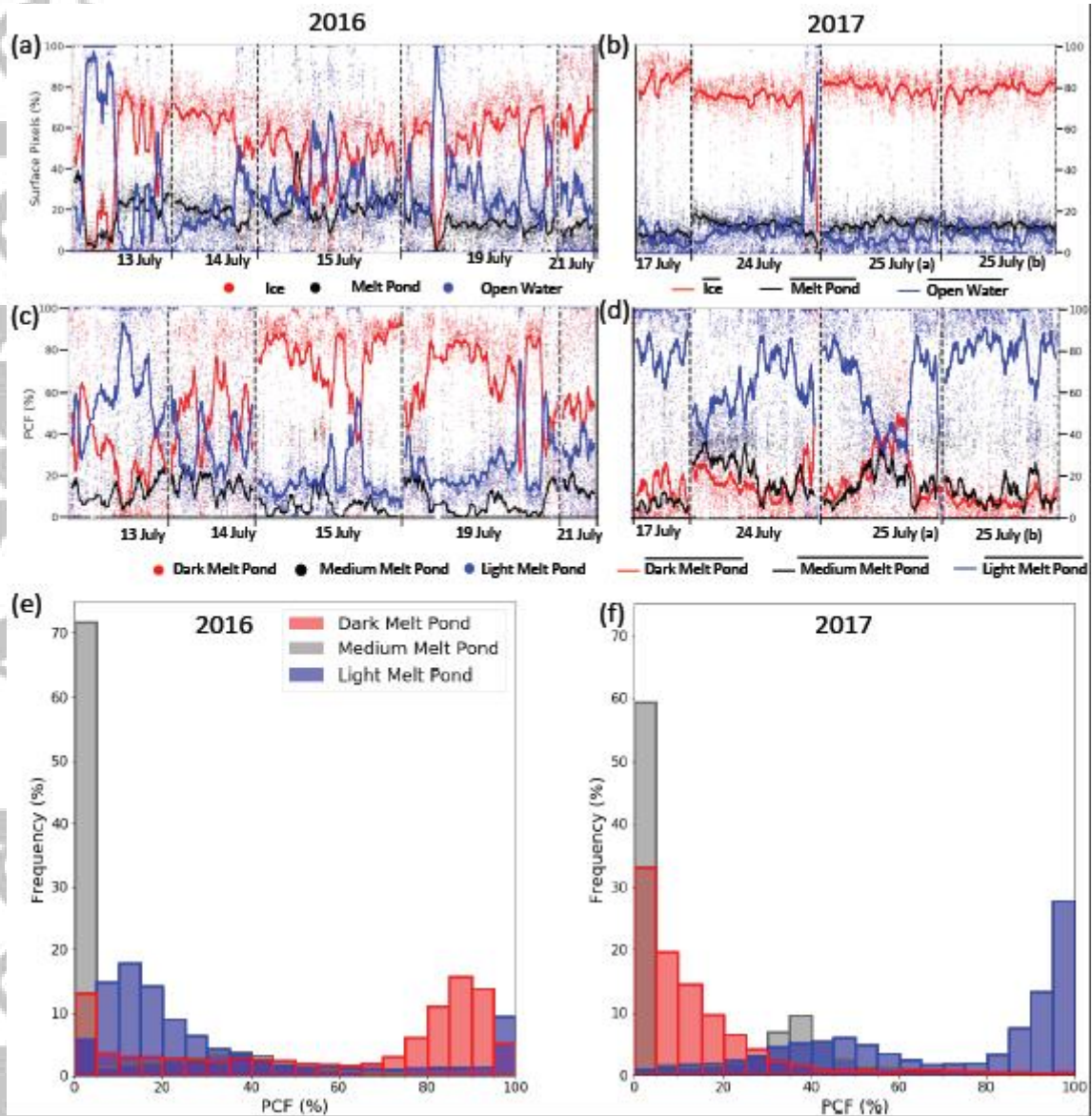


**Figure 11.** Results of image classification. (Top row) Percentage of surface pixels classified as ice (red dots), MP (black dots), and open water (blue dots) in 2016 (a) and 2017 (b), with running means calculated over 100 images (solid lines). Results are presented in chronological order, with vertical dashed lines (black) separating flights. (Middle row) PCF showing percentage dark (red), medium (black) and light (blue) MPs per image in 2016 (c) and 2017 (d). Solid and dashed lines same as in top row. (Bottom row) Frequency distributions of PCF for 2016 (e) and 2017 (f).

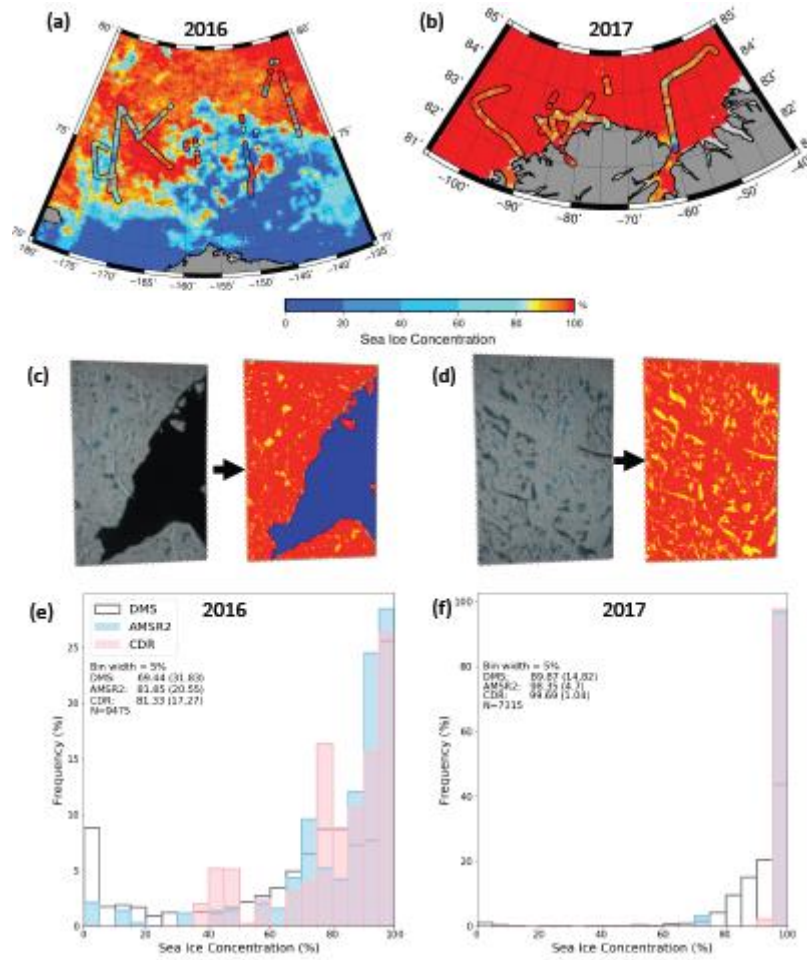


**Figure 12.** SIC results calculated per image. (a) DMS SIC overlaid on the AMSR2 SIC on July 17, 2016 and (b) July 21, 2017. (c) sample DMS images of sea ice in the Lincoln Sea on 24, July 2017 at  $-59.3^{\circ}\text{W}$ ,  $83.9^{\circ}\text{N}$  with relatively low SIC (65%) and (b)  $-59.6^{\circ}\text{W}$ ,  $83.4^{\circ}\text{N}$  with high SIC (100%). (e) frequency distributions of DMS SIC, AMSR2 SIC and CDR SIC, extracted at the same time and location of each DMS image acquisition in 2016 and (f) 2017.

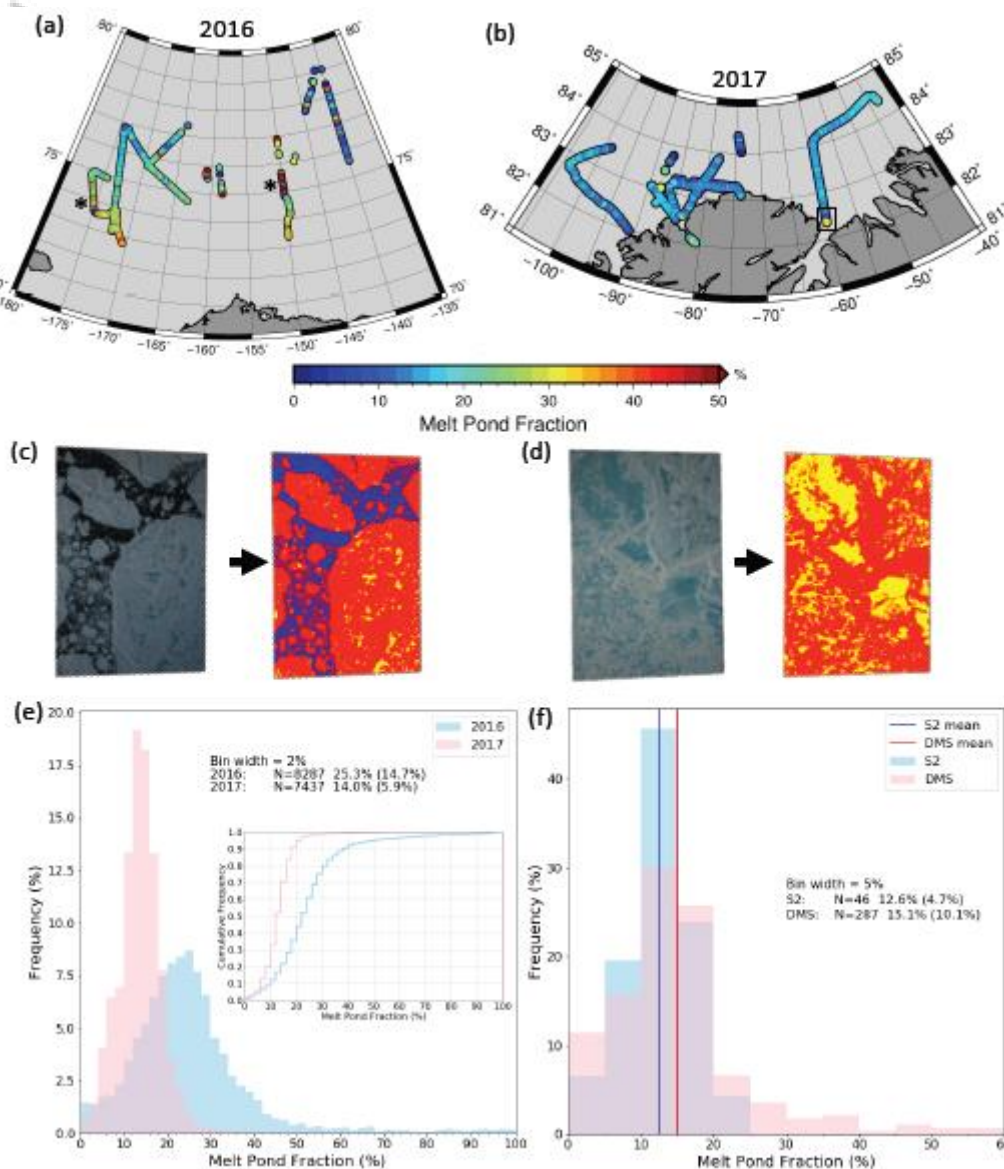


**Figure 13.** MPF results calculated per image. (a) MPF mapped for 2016, where \* marks area with anomalous MPF > 40% and (b) 2017, with the black box indicating the region compared with coincident Sentinel-2 imagery. (c) sample DMS images of sea ice in the Lincoln Sea acquired on 24, July 2017 at  $-59.6^{\circ}\text{W}$ ,  $83.3^{\circ}\text{N}$  with low MPF (17%) and (d)  $-59.9^{\circ}\text{W}$ ,  $82.6^{\circ}\text{N}$  with high MPF (50%). (e) Frequency distributions of MPF for 2016 (blue) and 2017 (pink). Inset is cumulative distribution of MPF for 2016 (blue curve) and 2017 (pink curve). (f) MPF distribution for coincident Sentinel-2 segments (light blue), DMS images (pink). The average MPF derived from Sentinel-2 strips and coincident DMS images is indicated by dark blue and red vertical lines, respectively.